

MSc Thesis in Life Science & Technology

Effect of Salts on Gas Bubble Sizes

Investigating the Role of Ion Redistribution Along the G/L-Interface to
Explain Bubble Coalescence Inhibition in Bubble Columns

Stijn Rommens
2024



Cover page: *Effervescence* by Debbie Kappelhoff

MSc Thesis in Life Science & Technology

Effect of Salts on Gas Bubble Sizes

**Investigating the Role of Ion Redistribution Along the G/L-Interface to
Explain Bubble Coalescence Inhibition in Bubble Columns**

Stijn Rommens

June 2024

A thesis submitted to Delft University of Technology in partial
fulfilment of the requirements for the degree of Master of
Science in Life Science & Technology

Stijn Rommens: *Effect of Salts on Gas Bubble Sizes* (2024)

© This work is licensed under a Creative Commons Attribution 4.0 International License.

To view a copy of this license, visit <http://creativecommons.org/licenses/by/4.0/>.

Cover page



Bioprocess Engineering
Delft University of Technology

Supervisors: Ir. Rik Volger
Dr. Ir. Cees Haringa

Committee: Dr. Bijoy Bera
Dr. Ir. Cees Haringa
Prof. Mark van Loosdrecht

Abstract

Recently, a mechanism has been proposed to describe how salts do (not) contribute to bubble coalescence inhibition. This is done by considering how ions (re)distribute themselves along the G/L-interface, expressing this as a Gibbs-Marangoni pressure. The thesis' goal is to investigate the potential and applicability of this mechanism to predict bubble coalescence inhibition for salts in biotechnological processes, specifically bubble columns.

This goal is achieved by recreating the mechanism and evaluating whether the Gibbs-Marangoni pressure is a better predictor than the ionic strength. To make this comparison, experiments are performed to study which ionic strengths/concentrations induce bubble coalescence inhibition. These numbers are then modelled in terms of Gibbs-Marangoni pressures, from where it is assessed which of the two better predicts this inhibition. Moreover, additional experimental results from the literature have been tested on the model to support this assessment.

The outcome of this thesis is a combination of multiple interesting insights. First, the above mechanism is successfully reproduced into a model. This statement is supported by comparing the model's results with previous literature applying this mechanism, showing that results deviate less than 10% from each other.

Secondly, from the performed experiments, bubble coalescence inhibition by salts is observable at an average ionic strength of 47.82 mM. Using these results in the model shows that this inhibition happens at an average Gibbs-Marangoni pressure of 1312.91 Pa. However, the inhibiting salt concentrations from the experiments deviate by more than 168% compared to the literature. This difference can be caused by many factors, such as dissimilarities in the experimental setups used. It shows that the critical Gibbs-Marangoni pressure is dependent on these factors and therefore not entirely generalizable for all scenarios.

Finally, the model's results are validated by comparing whether the additionally calculated surface tensions deviate less than 10% from the literature. This showed resulting Gibbs-Marangoni pressures are valid for pure salts at concentrations from 0.02-1.50 M. However, the validity of the model for salt mixtures is questionable.

To conclude, the proposed mechanism can describe bubble coalescence inhibition for salts in bubble columns. However, its accuracy is debatable as the model's results cannot be validated for mixtures. This may require the inclusion of other ion contributions into the model, such as ion polarizability, solvation energy and ion-charge density. Hopefully, this brings us closer to better modelling the effect of salts, and other compounds, on bubble coalescence inhibition.



Acknowledgements

Throughout my master's thesis project, I received a great deal of support and help from other people.

I would first like to thank my daily supervisor (and bubble buddy), Rik Volger. Without your daily support, this project would be impossible. Your obsession with bubbles made me enthusiastic and motivated to keep working on my project. Not only did you provide me with help for my thesis, but you were also there to talk about less formal topics. Thanks for your time and patience to work with me!

Also, thanks to Cees Haringa, Bijoy Bera and Mark van Loosdrecht for participating in my thesis committee. Cees Haringa also supervised me during my project and your helpful feedback and discussions were very valuable to me.

Moreover, I would also like to thank my office mates with whom I survived the past 9 months. Being in the same boat kept us floating towards the very end of our project. Part of this also has to do with the coffee card, of course. We could not have survived without it.

Furthermore, thanks to the CASE group (and BPE in general) for welcoming me since the start of my project. Also, I owe a special shout-out to Pieter Brorens for printing my thesis.

Lastly, I would like to thank my friends and family for all the support they gave me throughout my studies. Even though you might not know what I exactly did during my project, you made it possible for me to clear my head and not think about bubbles all the time.

Contents

Abstract	v
Acknowledgements	vii
Acronyms	xv
Symbols	xvii
1 Introduction	1
1.1 Bubble Columns	1
1.2 Bubble Coalescence Inhibition	2
1.2.1 Surface Tension and Ionic Strength	2
1.2.2 Surface Excess	4
1.3 Research Gap & Project Scope	5
2 Theoretical Background	7
2.1 Gibbs-Marangoni Pressure	7
2.2 Measuring Techniques	10
2.2.1 Fibre Probe	10
2.2.2 Pressure Sensor	12
3 Materials & Methods	13
3.1 Model Specifications	13
3.2 Experimental Setup	14
4 Results & Discussion	17
4.1 Recreating the Model	17
4.1.1 Surface Excess	19
4.2 Experiments	20
4.2.1 Effect of Gas Flow	20
4.2.2 Effect of Salts	21
4.3 Combining the Model with Experimental Data	25
5 Conclusion	33
5.1 Recommendations	34
5.1.1 Experiments	34
5.1.2 Model	34
A Ionic Adsorption-Free Energy	39
B Pressure Sensor Calibration	41
C Bubble Size Distributions	43

Contents

D Experimental Workflow	47
E Critical Safety Assessment	49
E.1 Equipment	49
E.2 Materials & Solvents	49
F Fibre Probe Signal Disturbance	51
G Transition Concentration	55
H Surface Tension Validation	57
H.1 Pure Electrolytes	57
H.2 Electrolyte Mixtures	58
H.3 Concentrated Electrolytes	59

List of Figures

1.1	Schematic representation of a bubble column.	1
1.2	Schematic representation of the relationship between increasing concentration and surface tension of surface-depleted (orange) and surface-enhanced (yellow) salts.	3
1.3	Schematic representation of the situation where an induced electrostatic potential leads to ion redistribution.	4
1.4	Schematic representation of the case where no electrostatic potential also results in no ion redistribution.	4
2.1	Schematic representation of the differences between electrostatic potential and adsorption-free energy. Here, an $\alpha\beta$ -salt is shown.	8
2.2	Illustration of the optical fibre probe's measuring technique. A smaller and dashed line represents a lower laser intensity. The differences in laser refraction can be seen when the probe's tip is submerged in liquid (above) or gas (below).	10
2.3	Schematic of the optical fibre probe's voltage (blue) when a valid bubble is detected (signal within the green interval). The increasing voltage amplitude, due to the Doppler effect, is enlarged for clarity.	11
2.4	Illustration of the pressure sensor's measuring technique. The dashed line represents the sensor liquid height at both non-sparged (left) and sparged (right) situations. The resulting pressure/height difference from sparging eventually gives the gas fraction below the sensor.	12
3.1	Bubble column filled with tap water and sparged with air (left). The column and a jerry can (white) are placed in a drip tray (orange). The gas line (blue), pressure sensor (black cord) and fibre probe (yellow cord) are connected. A schematic representation of the column, together with dimensions, is shown on the right.	15
3.2	Evolution of the mean for valid bubble sizes (blue) and holdup (green) of a fibre probe measurement.	16
4.1	Reproduced adsorption-free energy profiles for the ions and conditions also used in Duignan (2021)	17
4.2	Recreated electrostatic potential profiles for the electrolytes which have also been modelled by Duignan (2021) at a concentration of 0.1 M.	18
4.3	Reproduced concentration profiles from Duignan (2021) at a bulk concentration of 0.1 M.	19
4.4	Effect of gas flow rate, the superficial gas velocity, on bubble size and velocity (left) and gas holdup (right) in water. Sizes and velocities are represented by the measurement's median and interquartile range.	20

List of Figures

4.5	Effect of salt concentration on median bubble size and interquartile range (left) and mean gas holdup (right). The open circle depicts the transition point, derived from the regression curve. NH_4Cl 's distinct marker represents the different fibre probe used.	22
4.6	Expressing the change in bubble size in terms of the Gibbs-Marangoni pressure.	25
4.7	Model's surface tensions compared to experimental values from Henry et al. (2007) (linear), Jones and Ray (1937) (non-linear) for K_2SO_4 and Jones and Ray (1941) (non-linear) for NaCl . The dark grey line represents the validity region where surface tensions deviate less than 10% from each other. The area of validity (light grey) implies that deviations are less than 10% from this surface tension onwards.	26
4.8	Effect of salts on the percentage of bubble coalescence in terms of ionic strength and Gibbs-Marangoni pressure. Data is from Craig et al. (1993) and Henry et al. (2007)	27
4.9	Model's surface tensions compared to experimental values from Henry et al. (2007) . The $\text{NaClO}_3 + \text{HClO}_4$ mixture originally has a negative surface tension gradient, but its absolute values are plotted as a logarithmic scale is used. The dark grey line represents the validity region where surface tensions deviate less than 10%.	28
4.10	Effect of "non-inhibiting" electrolytes on the percentage of bubble coalescence in terms of ionic strength and Gibbs-Marangoni pressure. Hydrated radii of ions are adjusted to obtain less spreading of Gibbs-Marangoni pressures. Data obtained from Christenson et al. (2008)	29
4.11	Model's surface tensions compared to experimental values from Henry et al. (2007) . Area of validity implies a model's deviation of less than 10% with literature.	30
A.1	Schematic representation of a square well adsorption-free energy.	39
B.1	The pressure sensor's calibration line (blue) is established from the measurements (green). This calibration makes it possible to convert the measured voltage into a water height.	41
C.1	Histogram of bubble sizes measured by the optical fibre probe.	43
C.2	Histogram of bubble sizes measured by the optical fibre probe.	44
C.3	Boxplot of bubble sizes measured by the optical fibre probe.	45
E.1	Risk assessment for salts used during experiments.	49
F.1	Effect of NH_4Cl concentration on bubble size (left) and gas holdup (right). Size measurements are represented by their median and interquartile range.	51
F.2	0.5 M solutions of the different NH_4Cl batches tested. From left to right: LabDiscounter (original), LabDiscounter (other batch), Thermo Scientific and Carl Roth.	51
F.3	Effect of salt concentration on bubble size (left) and gas holdup (right). Size measurements are represented by their median and interquartile range. The distinct marker represents a different fibre probe used.	53

List of Tables

3.1	Hydrated radius for all ions used in this work. The ion types have been obtained from Henry et al. (2007)	14
4.1	Overview of surface tension gradients, electrostatic potentials and Gibbs-Marangoni pressures obtained from Duignan (2021) and this work.	19
4.2	Overview transition concentrations and ionic strengths obtained from experiments.	23
4.3	Overview of transition concentration ranges at the 50% mark found in the literature, together with their deviation from experimental results in this work. A comprehensive table of literature data, with sources, can be found in Appendix G.	24
4.4	Overview of the transition Gibbs-Marangoni pressures.	25
4.5	Validity concentration ranges for different solutes. ⁱ higher concentrations were not tested by Jones and Ray (1937) and Jones and Ray (1941) . ⁱⁱ lower concentrations could not be validated from Christenson et al. (2008)	31
C.1	Probabilities from the normality test.	44
G.1	Overview of 50% transition concentrations obtained from literature, together with the measuring technique used to obtain this number. ⁱ Concentration at 95% inhibition. ⁱⁱ Concentration at 75% inhibition.	55
H.1	Comparing the model surface tensions for NaCl. The transition regime is represented by the values printed in bold.	57
H.2	Comparing the model surface tensions for K ₂ SO ₄ . The transition regime is represented by the values printed in bold.	57
H.3	Comparing the model surface tensions for NaClO ₃ + HClO ₄	58
H.4	Comparing the model surface tensions for NaAc + KClO ₃	59
H.5	Comparing the model surface tensions for KAc.	59

Acronyms

GHG	Greenhouse gas
CO ₂	Carbon dioxide
α	Surface-depleting
β	Surface-enhancing
mPBE	Modified Poisson-Boltzmann equation
ODE	Ordinary Differential Equation
BVP	Boundary Value Problem
IVP	Initial Value Problem
FIRK	Fully-implicit Runge-Kutta
TS	Thermo Scientific
CR	Carl Roth
PMMA	Polymethyl methacrylate

Symbols

Symbol	Definition	Value	Unit
h	Thickness of thin film between bubbles	10	[nm]
N_A	Avogadro's number	$6.022 \cdot 10^{23}$	[1/mol]
k_B	Boltzmann constant	$1.381 \cdot 10^{-23}$	[J/K]
T	Temperature	297.15	[K]
e	Elementary charge	$1.602 \cdot 10^{-19}$	[C]
ϵ_0	Vacuum's permittivity	$8.854 \cdot 10^{-12}$	[F/m]
ϵ_w	Water's permittivity	78.3	[F/m]
p_{GM}	Gibbs-Marangoni pressure		[Pa]
ϕ	Electrostatic potential		[mV]
G^{ads}	Adsorption-free energy		[J]
G_i^{ads}	Species adsorption-free energy		[J]
W_i	Species work		[J]
X	Constant energy value		[J]
$d\gamma$	Surface tension		[mN/m]
$\frac{d\gamma}{dc}$	Surface tension gradient		[mN/m.M]
$\frac{d\gamma}{dc_i}$	Species surface tension gradient		[mN/m.M]
c	Concentration		[M]
c_i	Species concentration		[M]
I	Ionic strength		[M]
Γ_i	Species surface excess		[M]
Γ_+	Cation surface excess		[M]
Γ_-	Anion surface excess		[M]
c_t	Transition concentration		[M]
z	Distance from G/L-interface		[Å]
a_h	Hydrated radius		[Å]
$a_{h,i}$	Species hydrated radius		[Å]
w	Width		[Å]
κ	Inverse Debye-Hückel length		[1/Å]
k	Perpendicular κ		[1/Å]
s	Inverse spherical distance from κ & k		[1/Å]
f_D	Doppler frequency		[Hz]
λ_0	Vacuum's wavelength		[nm]
$h_{L, sparged}$	Sparged liquid height		[m]
$h_{L, non-sparged}$	Non-sparged liquid height		[m]
h_{sensor}	Sensor height		[m]
v	Bubble velocity		[m/s]
α	Bubble approaching angle		[°]
n_{ext}	Air's refractive index		[-]
q_i	Species charge		[-]
ϵ	Gas holdup		[-]

1 Introduction

The escalating issue of global warming has prompted a growing concern for lowering greenhouse gas (GHG) emissions and advancing sustainability to move to a carbon-neutral economy. As fossil fuel reserves are depleting, the need to explore alternatives for the petrochemical industry becomes larger. Industrial biotechnology presents itself as a promising field to pursue a sustainable, carbon-neutral economy. This is because bioprocesses do not require finite resources, like fossil fuels. Furthermore, biotechnology can even be used to convert GHGs, such as carbon dioxide (CO_2), into more valuable products (Hermann et al., 2007) (Köpke and Simpson, 2020). The effectiveness of such gas fermentations depends on sufficient mass transfer capacity of gaseous compounds into the liquid phase (Torli et al., 2018). Insufficient mass transfer prevents a microorganism from converting these gases into valuable products. This mass-transfer bottleneck can be reduced by using bubble columns and airlift reactors as they provide a more interfacial area between the gas and liquid phase, therefore increasing the mass transfer. These units are typically used in industry due to their cost-effectiveness and operational simplicity (Stoll et al., 2020).

1.1 Bubble Columns

Bubble columns, as depicted in Figure 1.1, introduce gas at the column's base through a sparger. This creates a flow where gas bubbles ascend through the liquid (Leonard et al., 2015). The airlift's compartments even allow the liquid and gas to recirculate in the reactor. During the transit, gas and liquid come into contact, facilitating the transfer of compounds between the two phases. In the liquid phase, microorganisms can uptake and convert these compounds into valuable products like acids or alcohols (Stoll et al., 2020) (Köpke and Simpson, 2020).

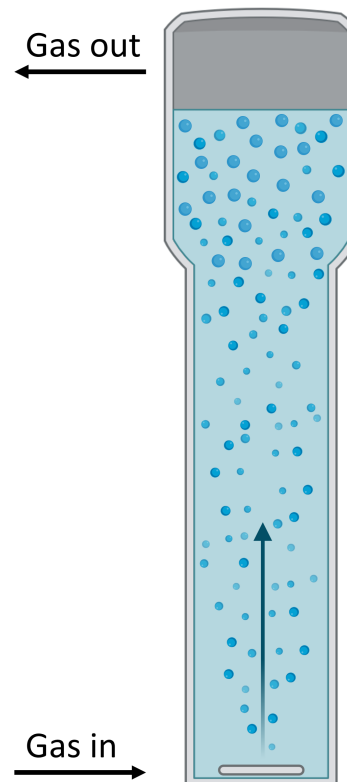


Figure 1.1: Schematic representation of a bubble column.

Besides substrate consumption and product generation, the fermentation process also involves other compounds to make the environment more favourable for the microorganism. For example, salts are added to provide essential nutrients for biomass growth. In the end, the fermentation broth is a complex liquid containing compound solutes such as acids, biomass and salts. Due to the presence of these compounds, the dynamics inside the column will also be different from a simple air-water system. An important consequence of altering the dynamics is that this can result in bubble coalescence inhibition, preventing gas bubbles from merging as they travel through the liquid. If bubbles cannot merge, the average bubble size will be smaller. This means an increase in interfacial area between the gas and liquid phase, which increases the mass transfer capacity of the system. This, of course, affects the performance of the microorganisms and the bioprocess as a whole (Volger et al., 2024).

When designing and scaling up such a bioprocess, this performance needs to be studied to see what column size is required to make the desired amount of product. Simulations are typically done to achieve such estimations. These simulations can be done as simple 1D models (Heijnen and Van't Riet, 1984) (Ngu et al., 2022) or as a more complex computational fluid dynamics simulation (Bhole et al., 2008) (Zhang and Luo, 2023). Even though these modelling techniques are all different, they do suffer from similar issues. Namely, these simulations are being done by presuming the column is an air-water system (McClure et al., 2015) (Puiman et al., 2022) and/or having bold assumptions on key parameters, such as gas bubble size (Zhang and Luo, 2023) (Puiman et al., 2022). This causes the simulated performance to be very different from reality. To resolve this issue, the difference in dynamics between broth and water needs to be known (Volger et al., 2024). As mass transfer capacity is often the bottleneck in gas fermentations, it is critical to understand the mechanism behind bubble coalescence inhibition.

1.2 Bubble Coalescence Inhibition

For bubbles to coalesce, they first need to bounce into each other. Then, the duration of their contact should be long enough before the bubbles bounce away from each other again. This is because a thin film forms when the bubbles come together, which also needs to drain before the bubbles can merge. This drainage is accomplished due to sufficient capillary pressure (Firouzi et al., 2015). If this layer cannot drain, bubble coalescence is inhibited (Sujan and Vyas, 2018). Previous attempts tried to express this inhibition by not considering the complexity involved with such processes, but this oversimplification shows to be insufficient. Therefore, a straightforward but sufficient understanding remains to be found.

1.2.1 Surface Tension and Ionic Strength

One of the earlier proposed mechanisms for inhibition is the Gibbs-Marangoni pressure (p_{GM}) by Marrucci (1969). Here, bubble coalescence is inhibited due to sufficient p_{GM} counteracting the capillary pressure (Firouzi et al., 2015). This p_{GM} is caused by a surface tension gradient, which is the difference in tension between the bulk liquid and the film (Marrucci, 1969). The surface tension is the force that describes the tendency of liquid surfaces to shrink into the minimum surface area possible. If the surface tension in the film is higher compared to the bulk, the liquid will flow from the bulk to the film. Instead of draining the film, this intrigues the film to be formed. This eventually prevents two bubbles from coalescing. This mechanism serves as a satisfactory explanation for inhibition by most salts. However, not all salts behave the same as their functioning depends on the ions they are composed of. According to Craig et al. (1993), ions can be characterised as being surface-depleting (α) or surface-enhancing (β). This characterisation is important as these two types of ions have different effects on the overall surface tension.

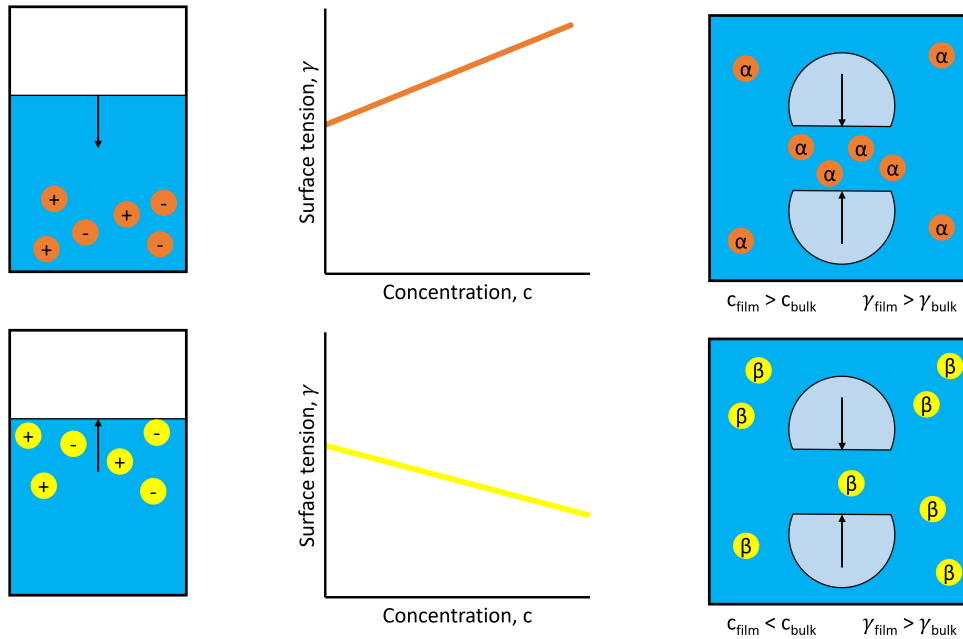


Figure 1.2: Schematic representation of the relationship between increasing concentration and surface tension of surface-depleted (orange) and surface-enhanced (yellow) salts.

The characteristic of $\alpha\alpha$ salts is that its ions tend to move away from the G/L-interface as interacting with the water is preferred. Moreover, these salts cause an increase in surface tension as their concentration increases. During bubble coalescence, the water moves away from the fluid film. However, due to the close contact of the two bubbles in the film, it is more difficult for α ions to escape. Therefore, relatively more ions are removed from the G/L-interface section which is not part of the film. This causes the salt concentration to be larger in the film than in the bulk. This increased concentration results in a higher surface tension at the film than at the bulk, inducing the backflow of liquid. This causes bubble coalescence inhibition to occur (Liu et al., 2023). Unlike $\alpha\alpha$ salts, $\beta\beta$ salts tend to interact more with the G/L-interface and are characterised by showing a decrease in surface tension as their concentration increases. As these ions spread out over the G/L-interface, the ionic concentration at the fluid film will be smaller than the bulk. Therefore, this will still result in a higher surface tension in the film compared to bulk. This shows that $\beta\beta$ salts also cause coalescence inhibition (Liu et al., 2023).

As mentioned, this mechanism works sufficiently enough for $\alpha\alpha$ and $\beta\beta$ salts. However, the explanation of other salts does not work as well with this mechanism. There are two important observations which appear to be inconsistent:

- Salts composed of surface α and β ions do not cause bubble coalescence inhibition when only one salt ($\alpha\beta$ or $\beta\alpha$) is used (Duignan, 2021).
- When a mixture of $\alpha\beta$ and $\beta\alpha$ salts is used, this suddenly does cause inhibition (Duignan, 2021).

Moreover, literature shows that straightforwardly using the salt concentration or ionic strength as an indicator also does not work (Craig et al., 1993) (Henry et al., 2007). These inconsistencies, together with the increasing interest in gas fermentation, urge the search for a more complete mechanism to describe this phenomenon.

1.2.2 Surface Excess

To explain why single $\alpha\beta$ or $\beta\alpha$ solutes do not cause inhibition, Duignan (2021) proposed a mechanism to obtain p_{GM} by taking the ion's surface excess into account rather than the surface tension gradient. When one of these salts is added to the system, their ions move either towards the surface or the bulk liquid. However, as these ions are differently charged, a charge separation is introduced. This separation is known as the electrostatic potential (ϕ). As the system wants to satisfy the electro-neutrality condition, ϕ drives the ions to redistribute themselves in the liquid. This results in α and β ions being mixed (Figure 1.3), which causes the ionic concentrations to be the same in the film and bulk. As there is no difference in surface excess, p_{GM} will be small. So, (almost) no bubble coalescence inhibition.

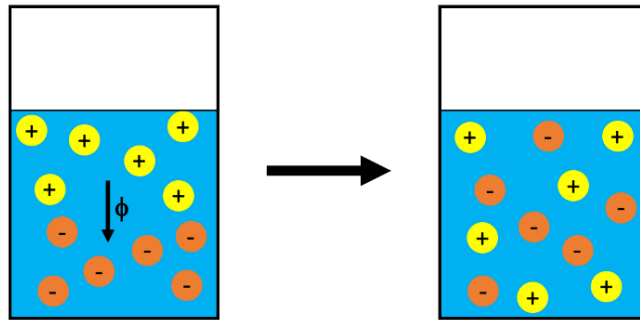


Figure 1.3: Schematic representation of the situation where an induced electrostatic potential leads to ion redistribution.

When using a mixture of $\alpha\beta$ and $\beta\alpha$ salts, the α and β are separated without introducing significant ϕ . This results in much less mixing of ions (Figure 1.4). Therefore, there is a difference in ionic excess between the film and bulk liquid, leading to a higher p_{GM} . So, more likely to have bubble coalescence inhibition.

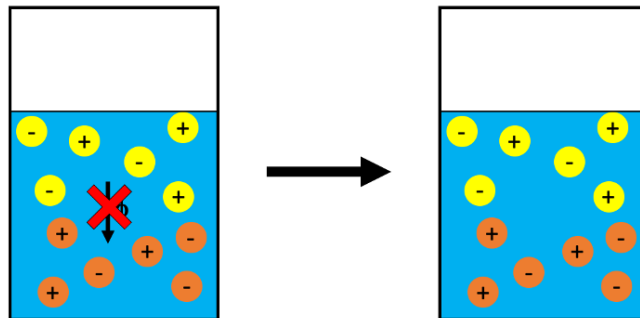


Figure 1.4: Schematic representation of the case where no electrostatic potential also results in no ion redistribution.

According to Duignan (2021), the surface excess is also dependent on the adsorption-free energy (G^{ads}). This energy accounts for the interaction strength between the ions and G/L-interface (Rosenholm, 2017). Combining G^{ads} and ϕ , the surface excess can be obtained more accurately. This results in a better estimation of bubble coalescence inhibition.

1.3 Research Gap & Project Scope

The work of Duignan (2021) gives a new mechanism to describe bubble coalescence inhibition by salts. This mechanism considers the electrostatic potential ϕ and adsorption-free energy G^{ads} introduced by every ion to obtain the Gibbs-Marangoni pressure p_{GM} , which can serve as an indication for bubble coalescence inhibition. The advantage of this mechanism is that it takes the effect of every different ion into account. This allows for not only predicting single salts but even mixtures of salts. In Duignan's work, four different salts have been simulated at a concentration of 100 mM. These salts are NaCl, HCl, NaClO₄, and HClO₄. Besides modelling them individually, a mixture of HCl + NaClO₄ has also been tested. For all these cases, p_{GM} and surface tension increments have been calculated. These calculations showed that the p_{GM} for NaCl, HClO₄ and HCl + NaClO₄ is high (>2000 Pa) and that this is low (<300 Pa) for HCl and NaClO₄. These results are as expected when looking at the mechanism's fundamentals. However, to validate the accuracy of the model, the calculated surface tension increments have been compared to literature data. As these numbers correspond with each other (Duignan, 2021), this mechanism shows great potential to describe bubble coalescence inhibition by salts. However, further studies on this mechanism have not been performed yet. No other salts or concentrations have been tested to extend this model. This is unfortunate as this mechanism could be an important contribution to bubble column simulations.

Looking at the current limitations of simulation tools and the work of Duignan (2021), there is a clear research gap to be seen. On one side, bubble column simulations need to be made more accurate. Heroic assumptions, such as bubble sizes, need to be resolved. In other words, a more profound practice needs to be used for these simulations. On the other side of the research gap, Duignan (2021) shows a potential mechanism to describe bubble coalescence inhibition. As inhibition and bubble size are related to each other, knowing when coalescence is inhibited gives the ability to also estimate resulting bubble sizes. These sizes can then be used in bubble column simulations. By applying a more dynamic system to estimate bubble sizes, more accurate simulation results can be achieved. As the current mechanism has still not been researched extensively, its true potential remains unrevealed. There is a gap to be bridged between the current model and the future use of it in simulations. This leads to the following research question:

Considering ion redistribution along the G/L-interface due to electrostatic potential, does it contribute to accurately predicting bubble coalescence inhibition for salts?

To contribute to this research gap, the existing model from Duignan (2021) will be extended by testing more (mixtures of) salts to further validate the model. To test more salts, experiments are also performed to measure the effect of salts on bubble sizes, specifically for NaCl, NH₄Cl, Na₂SO₄ and (NH₄)₂SO₄. These salts are chosen because they allow the testing of every ion combination. To answer the research question, subquestions have been made:

- Do the recreated results from Duignan (2021) differ less than 10%?
- Do the experimental results vary not more than 10% from the literature?
- Combining the model with experimental data, is the model a good predictor and are its additionally calculated surface tensions deviating less than 10%, therefore valid?

It is desired to obtain a predictor which shows how and if different salts (mixtures) result in the same inhibition and, therefore, the same gas bubble size. In the future, this work can hopefully be used as a tool for more accurate bubble column simulations. This will bring research closer to properly simulating complex mixtures, such as fermentation broths.

2 Theoretical Background

Before the work from [Duignan \(2021\)](#) can be used, the underlying mechanism needs to be understood properly. This section presents and explains the foundation of this previously mentioned study by showing the necessary formulas and how they relate to each other. As this thesis also contains experimental work, the measurement principles are explained too.

2.1 Gibbs-Marangoni Pressure

The originally proposed mechanism by [Marrucci \(1969\)](#) proposed that the Gibbs-Marangoni pressure (p_{GM}) from a single species in a solvent is calculated from the total surface tension gradient ($\frac{d\gamma}{dc}$), species concentration (c), thickness of thin film between bubbles (h), Avogadro's number (N_A), Boltzmann constant (k_B) and temperature (T) (Equation 2.1).

$$p_{GM} = \frac{4c}{h^2 N_A k_B T} \left(\frac{d\gamma}{dc} \right)^2 \quad (2.1)$$

The principle can also be applied when multiple species are present by considering the individual species concentration (c_i) and surface tension gradients ($\frac{d\gamma}{dc_i}$) (Equation 2.2).

$$p_{GM} = \frac{4}{h^2 N_A k_B T} \sum_i c_i \left(\frac{d\gamma}{dc_i} \right)^2 \quad (2.2)$$

However, as also described in the [Introduction](#), the surface tension is shown to be inconsistent with experimental results. Hence, [Duignan \(2021\)](#) opted to calculate p_{GM} by considering the (re)distribution of ions at the G/L-interface. This is done by looking at the surface excesses of each species, which examines individual contributions. Therefore, Equation 2.2 needs to be rewritten. This can be done by considering the Gibbs adsorption isotherm as it describes how a change in surface tension ($d\gamma$) and concentration (dc_i) relates to a species' surface excess (Γ_i) (Equation 2.3).

$$-\frac{1}{N_A k_B T} d\gamma = \sum_i \frac{\Gamma_i}{c_i} dc_i \quad (2.3)$$

Isolating the surface tension gradient (Equation 2.4) from the Gibbs adsorption isotherm allows to substitute $\frac{d\gamma}{dc_i}$ with $\frac{d\Gamma_i}{dc_i}$ in Equation 2.2. Now, p_{GM} can be calculated without the need for individual surface tensions (Equation 2.5). Nevertheless, this relation still makes it possible to calculate the surface tension. This is useful to check the validity of the results by comparing it with the literature.

$$\frac{d\gamma}{dc_i} = -N_A k_B T \sum_i \frac{\Gamma_i}{c_i} \quad (2.4)$$

$$p_{GM} = \frac{4N_A k_B T}{h^2} \sum_i c_i \left(\frac{\Gamma_i}{c_i} \right)^2 \quad (2.5)$$

2 Theoretical Background

As can be seen in Equation 2.5, p_{GM} cannot be calculated before a surface excess is obtained. The definition of a species' surface excess is the difference between its local concentration at distance z from the G/L-interface in the liquid ($c_i(z)$) and the bulk concentration ($c_i(\infty)$) (Equation 2.6). A positive surface excess indicates that the species is more abundantly present at the interface compared to the bulk liquid. Considering salts, this indicates the ions are surface-enhanced (β -ions). Negative surface excess shows that the ions have surface-depleting properties (α -ions).

$$\Gamma_i = \int_0^{\infty} dz(c_i(z) - c_i(\infty)) + \int_{-\infty}^0 dzc_i(z) \quad (2.6)$$

A species concentration profile can be described by Equation 2.7, which takes into account (1) the system's total electrostatic potential ϕ and (2) the species adsorption-free energy G_i^{ads} over the distance. By also considering the species charge q_i , this equation accounts for whether the species is affected by the total electrostatic potential or not. This means that the model cannot only evaluate salts/ions but also non-charged compounds, such as alcohols. This underpins the model's applicability potential for complete fermentation broths.

$$c_i(z) = c_i(\infty) \exp \left[-\frac{1}{k_B T} \left(G_i^{ads}(z) + q_i \phi(z) \right) \right] \quad (2.7)$$

Besides the definition, ϕ and G_i^{ads} also differ in the sense that ϕ considers the total interaction between the different species themselves, whereas G_i^{ads} considers the individual interaction between a species and the G/L-interface. This difference is illustrated by extending the example from the Introduction (Figure 2.1).

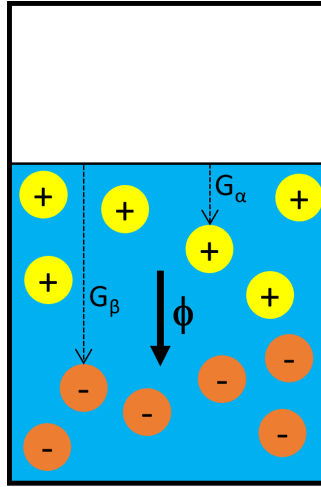


Figure 2.1: Schematic representation of the differences between electrostatic potential and adsorption-free energy. Here, an $\alpha\beta$ -salt is shown.

Electrostatic potential

To consider the total interaction between the species, using only a species' individual contribution is insufficient to obtain ϕ . To resolve this, the Poisson-Boltzmann equation is used as it describes the distribution of ϕ at any distance from the surface by summing up the contributions of all the species present (Equation 2.8). Here, ϵ_0 and ϵ_w represent the permittivity for vacuum and water and e the elementary charge.

$$-\epsilon_0\epsilon_w\frac{d^2\phi(z)}{dz^2} = e^2\frac{N_A}{k_B T}\sum_i q_i c_i(z) \quad (2.8)$$

Combining Equations 2.7 and 2.8 gives the modified Poisson-Boltzmann equation (mPBE) (Equation 2.9). The inclusion of G_i^{ads} is what makes this equation modified compared to the standard Poisson-Boltzmann equation, where this term is ignored.

$$\frac{d^2\phi(z)}{dz^2} = -\frac{e^2}{\epsilon_0\epsilon_w}\frac{N_A}{k_B T}\sum_i q_i c_i(\infty)\exp\left[-\frac{1}{k_B T}\left(G_i^{ads}(z) + q_i\phi(z)\right)\right] \quad (2.9)$$

Adsorption-free energy

As the adsorption-free energy considers a species' individual interaction with the G/L-interface, it allows different G_i^{ads} -functions to be used from species to species. This allows the mechanism to model every species as accurately as possible. As this thesis only contains experimental work with α -ions, this G_i^{ads} -function will be shown to serve as an explanation. However, different functions for different species can be found in Appendix A.

An α -ion's interaction is made up of a long-range image charge electrostatic repulsion combined with a hard repulsive wall (Equation 2.10). According to Duignan (2021), the hard repulsive wall is a standard approximation for modelling ionic interactions that capture the strong hydration shell of these ions. The G_i^{ads} -related functions used are the same function developed by Levin et al. (2009) and dos Santos and Levin (2010). This function states that an α -ion's adsorption energy, at distances z shorter than its hydrated radius $a_{h,i}$, has significantly high energy due to its hard repulsive wall. This is because (part of) the ion can never be present in the gas phase. At larger distances, G_i^{ads} relies on (1) the work W_i required to bring the ion from the G/L-interface to z and (2) the ion's net electrostatic effect into the bulk liquid (the inverse Debye-Hückel length, κ).

$$G_{\alpha,i}^{ads}(z) = \begin{cases} \frac{W_i a_{h,i}}{z} \exp[-2\kappa(z - a_{h,i})], & \text{for } z \geq a_{h,i} \\ 1000k_B T, & \text{for } 0 < z < a_{h,i} \end{cases} \quad (2.10)$$

The required work W_i is calculated by taking the integral over k , the perpendicular direction of κ (Equation 2.11). This is done to account for the ion's effect along the G/L-interface. It can be seen that the integral also takes s , which only consists of k and κ (Equation 2.12).

$$W_i(z; a_{h,i}) = \frac{q^2 e^2}{8\pi\epsilon_0\epsilon_w} \int_0^\infty dk \frac{k(s \cosh(ka_{h,i}) - k \sinh(ka_{h,i}))}{s(s \cosh(ka_{h,i}) + k \sinh(ka_{h,i}))} \quad (2.11)$$

$$s = \sqrt{\kappa^2 + k^2} \quad (2.12)$$

2 Theoretical Background

To determine how far into the bulk liquid the ions have an electrostatic effect, κ is calculated (Equation 2.13). This is done by considering the total ionic strength (I) of the liquid (Equation 2.14).

$$\kappa = \sqrt{\frac{2e^2 N_A I}{k_B T \epsilon_0 \epsilon_w}} \quad (2.13)$$

$$I = \frac{1}{2} \sum_{i=1}^n c_i z_i^2 \quad (2.14)$$

2.2 Measuring Techniques

As for the experiments, two measuring devices are being used, an optical fibre probe and a pressure sensor. The fibre probe is used to measure the individual bubble size and velocity. Moreover, it quantifies the void fraction in the liquid, also known as the gas holdup. To do this, the bubble needs to be pierced by the probe's tip. The pressure sensor, indirectly, also measures a holdup. This is achieved by measuring a voltage signal, which can be related to a change in water level due to the gas present in the liquid. The big difference between the two measurements is that the fibre probe only considers the local holdup, whereas the pressure sensor measures the global holdup under the probe.

2.2.1 Fibre Probe

To measure the bubble size, velocity and local gas holdup, the probe needs to be able to differentiate between the gas and liquid phase. This is being done by sending a laser signal to the probe's tip. Based on the refraction of the laser, the two phases are distinguished (Figure 2.2). The reason is that air results in refraction which is at least ten times higher compared to when the probe's tip is submerged in liquid (van der Bom, 2023).

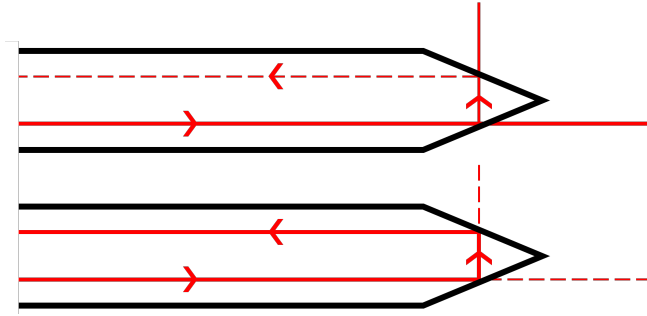


Figure 2.2: Illustration of the optical fibre probe's measuring technique. A smaller and dashed line represents a lower laser intensity. The differences in laser refraction can be seen when the probe's tip is submerged in liquid (above) or gas (below).

The measuring device also contains a potentiometer to adjust the laser's intensity. This makes it possible to control the laser power sent to the probe's tip. As the ingoing signal is known, the refracted signal can also be quantified. Sufficient laser power is required to make a clear distinguishment between the gas and liquid phases. When these two phases can be identified by the probe, the gas holdup is easily obtained by measuring the time fraction when the tip is submerged in air. However, determining the bubble size and velocity requires a more complex procedure. First, these values can only be determined when the bubble is considered to be valid. This means that the measured voltage signal needs to have a crenel-like signal, such as in Figure 2.3.

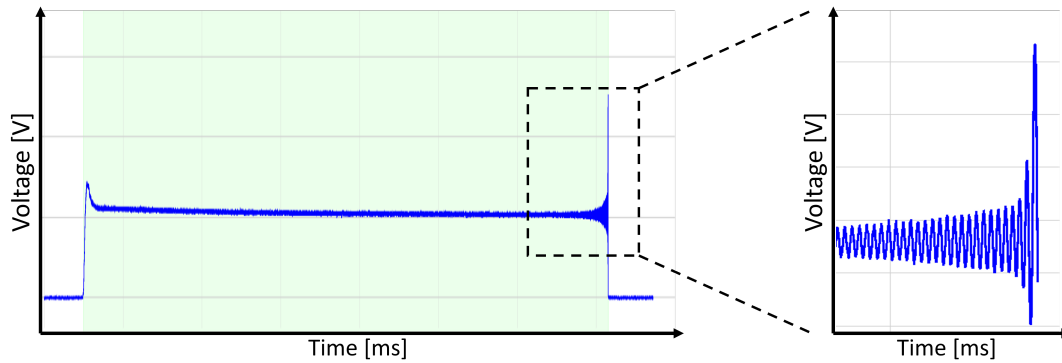


Figure 2.3: Schematic of the optical fibre probe's voltage (blue) when a valid bubble is detected (signal within the green interval). The increasing voltage amplitude, due to the Doppler effect, is enlarged for clarity.

Once a bubble is considered valid, its velocity is derived from the measured Doppler signal where the bubble is exiting the probe. This signal is a result of combining the laser refraction from (i.) the probe itself and (ii.) the approaching G/L-interface. The refracted frequency from the interface differs from the original, increasing the voltage amplitude. The bubble's exit signal is used as this voltage amplitude is more significant compared to the bubble's entering signal. This voltage signal, together with its frequency, is used to obtain the Doppler frequency f_D . From here, the bubble velocity v can be calculated (Equation 2.15). This is done by considering the angle α in which the bubble approaches the probe, the laser's wavelength in vacuum λ_0 and the air's refractive index n_{ext} .

$$f_D = 2 \frac{v \cos(\alpha)}{\lambda_0 / n_{ext}} \quad (2.15)$$

The bubble size is obtained when multiplying the velocity by its residence time, which is the time interval where the valid bubble is detected (Lefebvre et al., 2022).

2.2.2 Pressure Sensor

The pressure sensor is used to obtain the global gas holdup (ϵ). This is achieved by calculating the change in water height when sparged (Equation 2.16) (Bahri et al., 2013). This is done by taking the difference between the sparged water height ($h_{L, sparged}$) and its original height ($h_{L, non-sparged}$). However, the sensor does not directly return these heights. Instead, it measures a voltage. This voltage represents how much pressure the sensor perceives. As the water level rises, due to gas being present in the liquid phase, the pressure experienced by the sensor increases too. The measured voltage signal can therefore be correlated with the liquid height. To do this, the sensor must first be calibrated (Appendix B).

$$\epsilon = \frac{h_{L, sparged} - h_{L, non-sparged}}{h_{sensor}} \quad (2.16)$$

Equation 2.16 and the schematic representation of the changing liquid height (Figure 2.4) show that the pressure sensor is not used to calculate the gas holdup of the complete liquid phase. Alternatively, it only considers the holdup of the liquid volume that originally was below the sensor's height level (h_{sensor}). This is important to point out as the sensor cannot be used to measure how much gas is above the sensor.

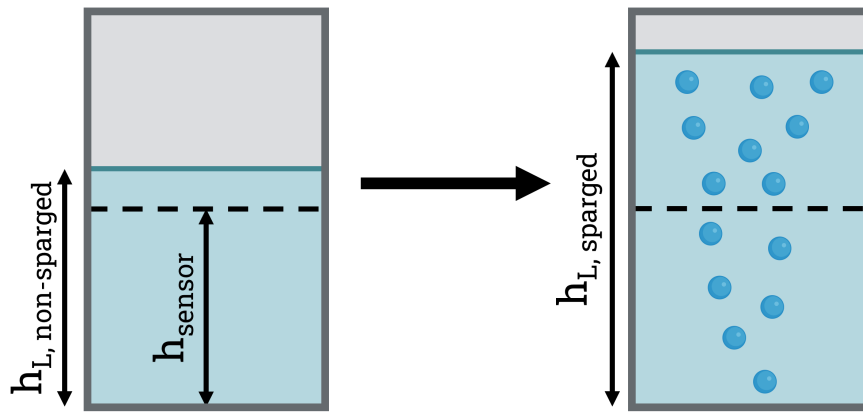


Figure 2.4: Illustration of the pressure sensor's measuring technique. The dashed line represents the sensor liquid height at both non-sparged (left) and sparged (right) situations. The resulting pressure/height difference from sparging eventually gives the gas fraction below the sensor.

Moreover, it needs to be noted that additives influence the voltage signal to the liquid. As this work looks at the influence of salts on bubbles, the addition of salts to the liquid can affect the density and height of the liquid. These system changes need to be corrected when calculating the water height. This can be achieved by measuring the voltage difference at the experiment's beginning and end when the column is not being sparged.

3 Materials & Methods

3.1 Model Specifications

The [Theoretical Background](#) shows that the electrostatic potential (ϕ) and adsorption-free energies (G_i^{ads}) are needed to calculate the Gibbs-Marangoni pressure, p_{GM} . To obtain these numbers, the model is made in Julia (v1.9.3) to allow for faster calculation times compared to Python. However, this increase in speed is only valuable when the results are valid. Therefore, to see if the model is solved correctly, it is checked whether the electroneutrality condition is satisfied (Equation 3.1). This condition states that the total cation (Γ_+) and anion (Γ_-) surface excesses need to be equal. The control step is mandatory as electroneutrality, due to the redistribution of ions, is enforced by ϕ . Calculations not fulfilling this condition imply that the resulting p_{GM} is not justifiable.

$$\frac{\partial \gamma}{\partial c_+} = -N_A k_B T \frac{\Gamma_+}{c_+} = -N_A k_B T \frac{\Gamma_-}{c_-} = \frac{\partial \gamma}{\partial c_-} = \frac{1}{2} \left(\frac{d\gamma}{dc} \right) \quad (3.1)$$

Moreover, the aforementioned condition relates the surface excesses to the surface tension. This relation explains why the total surface tension can be correlated with bubble coalescence inhibition. However, as also mentioned in the [Introduction](#), this correlation is only valid to pure electrolytes and not to electrolyte mixtures.

Electrostatic potential

To calculate ϕ , the modified Poisson-Boltzmann equation (mPBE) needs to be solved (Equation 2.9). This is a second-order ordinary differential equation (ODE) to the following standard boundary conditions have been applied:

- Zero electrostatic field in the vacuum ($\frac{d\phi(z)}{dz}=0$).
- Zero electrostatic potential in bulk liquid ($\phi(\infty)=0$).

This implies that no ions are present in the gas phase and that all ions are perfectly mixed in the bulk liquid. The above conditions are considered to be standard as these are generally used when looking at distributions and potentials at interfaces ([Uematsu et al., 2018](#)) ([Duignan et al., 2018](#)) ([Duignan, 2021](#)).

Adsorption-free energy

The G_i^{ads} requires the ion's bulk concentration (c_i) and hydrated radius ($a_{h,i}$) as parameters. The bulk concentration is easily acquired from experiments and literature. However, obtaining a_h from literature has shown to be difficult as this value is different between studies. Moreover, no study or database lists all the ions used in this work. Therefore, if possible, a_h for ions have been collected from [dos Santos and Levin \(2010\)](#). Using this source makes it possible to recreate the results from [Duignan \(2021\)](#). When an ion is absent in this database, its a_h is estimated based on the Hofmeister series (Table 3.1). This series is chosen as an approximation because it orders ions based on their capacity to adsorb water, therefore influencing a_h ([Gregory et al., 2022](#)).

Table 3.1: Hydrated radius for all ions used in this work. The ion types have been obtained from [Henry et al. \(2007\)](#).

Ion	Type	Hydrated radius	Source
Mg ²⁺	α	4.28 Å	-
Ca ²⁺	α	4.12 Å	-
H ⁺	β	1.97 Å	(dos Santos et al., 2010)
Na ⁺	α	2.50 Å	(dos Santos and Levin, 2010)
K ⁺	α	2.40 Å	-
NH ₄ ⁺	α	2.30 Å	-
ClO ₄ ⁻	β	2.83 Å	(dos Santos and Levin, 2010)
ClO ₃ ⁻	β	2.16 Å	(dos Santos and Levin, 2010)
NO ₃ ⁻	α	1.98 Å	(dos Santos and Levin, 2010)
Cl ⁻	α	2.00 Å	(dos Santos and Levin, 2010)
CH ₃ COO ⁻	β	3.22 Å	-
SO ₄ ²⁻	α	3.79 Å	(dos Santos and Levin, 2010)

3.2 Experimental Setup

For the experiments, the influence of four different salts on gas bubble sizes is tested. These salts are NaCl, NH₄Cl, Na₂SO₄ and (NH₄)₂SO₄ and are all from LabDiscounter, with a purity of $\geq 99\%$. Moreover, additional NH₄Cl batches from Thermo Scientific (TS) and Carl Roth (CR) are tested. These have the same purity as other salts.

To study the influence of salts on bubble sizes, experiments are performed in a polymethyl methacrylate (PMMA) column with a porous sparger plate. This column has a diameter of 15.0 cm (Figure 3.1) and was chosen due to its availability. Even though a porous plate is used, the small volume underneath results in the sparger producing more bubbles at the far side of the gas inlet. This is because the incoming gas is not able to equally distribute and pressurize under the sparger. The produced flow pattern does cause variation in measurements along the radial axis, but can be corrected for as this flow is static. This makes it possible to still compare different experimental results.

As mentioned in [Theoretical Background](#), measurements are performed with an optical fibre probe and pressure sensor. Both these devices are located at a height of 74.8 cm, while the water height is at least 90.0 cm from the bottom (Figure 3.1). This height difference prevents the top water layer from influencing the fibre probe's measurement. As gas holdup and bubble breakups increase at the top zone of the column, this results in inaccuracies and fluctuations when investigating the effect of salts on bubble coalescence ([Esmaeili et al., 2015](#)).

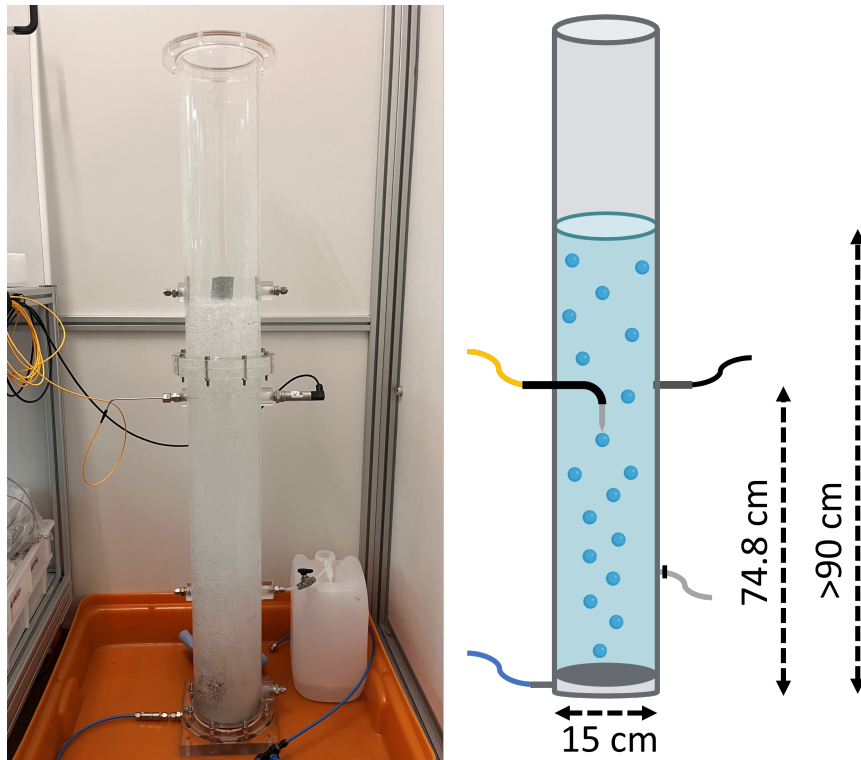


Figure 3.1: Bubble column filled with tap water and sparged with air (left). The column and a jerry can (white) are placed in a drip tray (orange). The gas line (blue), pressure sensor (black cord) and fibre probe (yellow cord) are connected. A schematic representation of the column, together with dimensions, is shown on the right.

Measuring devices

The optical fibre probe "M2 Bubbly Flow Analyzer" and corresponding computer software "M2 Analyzer for Bubble flows" (v2.34) from A2 Photonic Sensors are used to measure the gas holdup, bubble size, and bubble velocity. The fibre probe is placed in the column such that the probe's tip is pointing downwards, perpendicular to the sparger plate. The holdup is determined by measuring over a total time interval of 30 seconds. Halfway through the experiments, holdup measurements are done over a time interval of 120 seconds to obtain more stable measurements. To get an accurate reading on bubble size and velocity, it has been chosen that 4000 blocks need to be measured. Depending on the probe's validation rate, this results in 700-1000 valid bubbles measured. This specific time interval and number of blocks are chosen as this results in stabilisation of the mean measurements (Figure 3.2). Even though Figure 3.2 considers the mean of a probe's measurement, the median better represents the data (Appendix C). The reason is that velocity and size measurements return large distributions. Moreover, statistical tests show that this data is not (log-)normally distributed. As a result, the mean could vary significantly between different measurements. As the median is less sensitive to wide distributions and outliers, this value is more consistent for comparisons (Sainani, 2012). Therefore, the median is considered for further data visualisation.

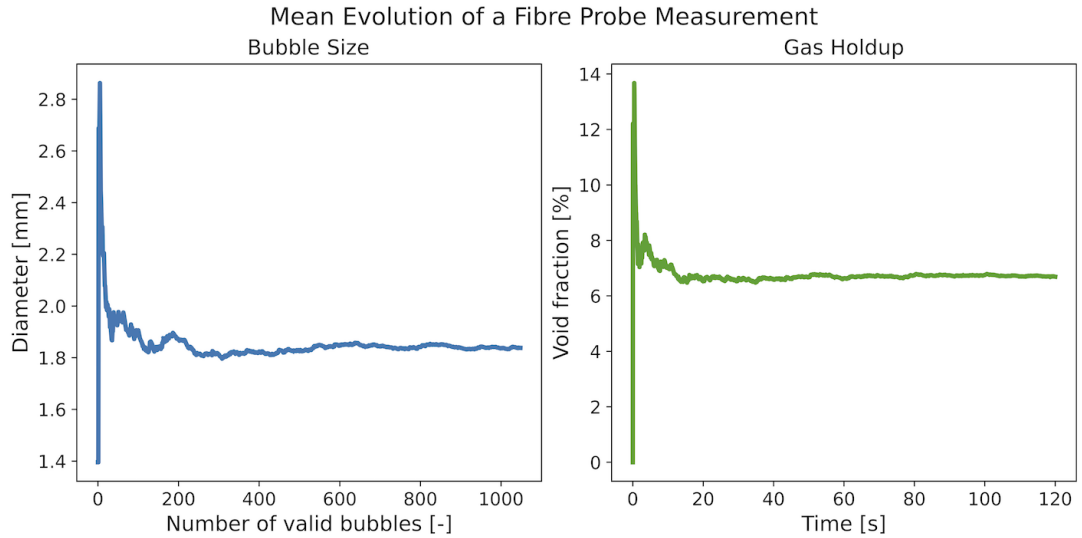


Figure 3.2: Evolution of the mean for valid bubble sizes (blue) and holdup (green) of a fibre probe measurement.

The pressure sensor PXM419-070HG10V from Omega is used for additional gas holdup measurements. This sensor is connected to the NI USB-6009 device from National Instruments to log the measured voltage via NI LabView (2018 SP1) on a computer. The voltage is logged during the entire period when the fibre probe is measuring as well. This voltage is converted to the column's water height by using the calibration line from Appendix B.

Air supply

The gas is regular air from outside, delivered to the column from a compressor. The air supply is regulated with the F-202AC-AAB-55-V mass flow controller by Bronkhorst, together with the software FlowDDE (V4.84) and FlowView 3 (V1.23). Before entering the column, the air needs to pass a one-way valve. This valve is connected to the column to prevent liquid from running back into the gas system. During experiments, the airflow rate is kept constant at 20 L/min. With the column dimensions, this is equal to a superficial gas velocity of 1.89 cm/s. This is the maximum achievable rate while preventing overfoaming of the column at the water height used.

To combine the column with the measuring devices and regulators, an experimental workflow has been made (Appendix D). This workflow provides instructions for both setting up and performing the experiments. Moreover, a safety assessment is performed to evaluate the risks of the experiments performed (Appendix E).

4 Results & Discussion

4.1 Recreating the Model

Before the mechanism presented in the [Introduction](#) can be tested, the model from [Duignan \(2021\)](#) needs to be recreated. This is done by first reproducing the adsorption-free energies and electrostatic potentials of the modelled electrolytes (NaCl, NaClO₄, HCl, HClO₄ and HCl + NaClO₄) at a concentration of 0.1 M. G_i^{ads} is reproduced by using the Heaviside step functions shown in the [Theoretical Background](#) and [Appendix A](#). Using the ion's designated function, together with its accompanied hydrated radius, the results from [Duignan \(2021\)](#) are duplicated ([Figure 4.1](#)).

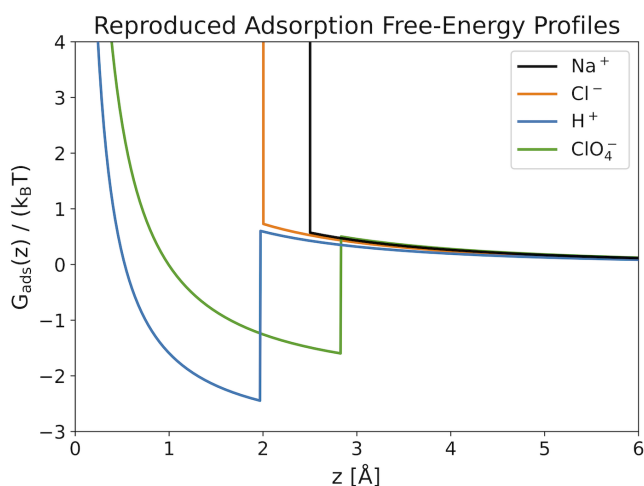


Figure 4.1: Reproduced adsorption-free energy profiles for the ions and conditions also used in [Duignan \(2021\)](#).

These energy profiles are used in the mPBE to obtain $\phi(z)$ of the system. However, treating the ODE as a boundary value problem (BVP) with the conditions given in the [Materials & Methods](#) ($\frac{d\phi(0)}{dz}=0$ and $\phi(\infty)=0$) does not return the desired outcome. The reason is that these boundary conditions will already be fulfilled if $\phi=0$ over the entire distance. Even though the ODE is solved, this may not always satisfy the electroneutrality condition as ions will never be redistributed in this scenario. This issue has been resolved by applying a different technique for solving ODEs, the shooting method.

Shooting transforms the BVP into an equivalent initial value problem (IVP). It allows the solver to still roughly comply with the system's boundaries while also changing its initial conditions. As initial values are required for this method to work, these conditions must also be passed to the solver. However, as shown by Duignan (2021), $\phi(0)$ can vary significantly between different electrolytes. Predicting $\phi(0)$ as an initial value is therefore difficult and inefficient for the shooting method. To overcome this problem, the mPBE has been reversed (Equation 4.1). Now distance $z=0$ is not at the G/L-interface anymore, but in the bulk liquid. The initial conditions at this region are more predictable due to ϕ 's depletion in the bulk, which results in $\frac{d\phi(\infty)}{dz}=0$ and $\phi(\infty)=0$.

$$\frac{d^2\phi(z)}{dz^2} = -\mathbf{1} \cdot -\frac{e^2}{\epsilon_0\epsilon_w} \frac{N_A}{k_B T} \sum_i q_i c_i(\infty) \exp \left[-\frac{1}{k_B T} \left(G_i^{ads}(z) + q_i \phi(z) \right) \right] \quad (4.1)$$

The shooting method itself is not enough to solve the mPBE. The right solver algorithm needs to be chosen too. This is because each algorithm solves a problem differently, which gives every solver its own (dis)advantages. Different algorithms are tested to see which returns a successful result while not being too time-consuming. Due to the stiffness of the problem, it turns out that a fully-implicit Runge-Kutta (FIRK) solver is the best to allow for accurate and efficient calculations, specifically RadauIIA5 from Julia's DifferentialEquations library. The absolute and relative tolerances are set at 10^{-15} to elevate the accuracy further. It needs to be noted that this algorithm normally also uses automatic differentiation to solve the problem. This is turned off to prevent too small time steps, which would otherwise result in the model not being solved. Solving the reversed mPBE with the conditions above results in the electrostatic potentials from Duignan (2021) being duplicated (Figure 4.2). Even though mPBE is reversed, the results are shown in such a way that $z(0)$ still represents the G/L-interface.

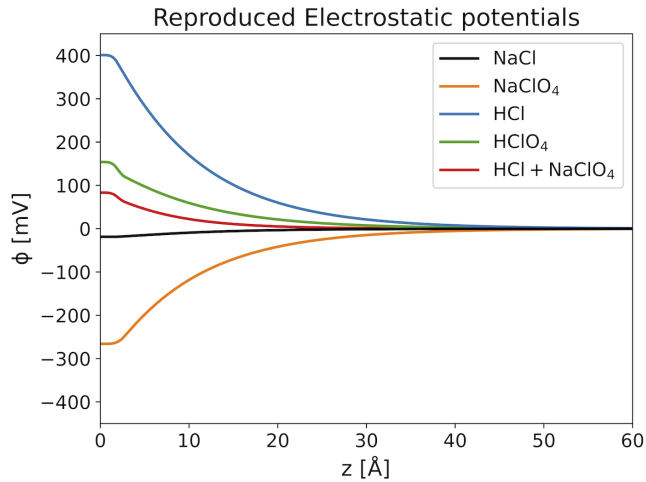


Figure 4.2: Recreated electrostatic potential profiles for the electrolytes which have also been modelled by Duignan (2021) at a concentration of 0.1 M.

The effectiveness of the shooting method can be evaluated by comparing the obtained boundary values with the previously mentioned boundary conditions. The results show that $\frac{d\phi(0)}{dz}$ and $\phi(\infty)$ are not completely equal to zero, but the solver still returns values very close to zero. These numbers are in the order of $\leq 10^{-7}$ from the applied tolerances.

4.1.1 Surface Excess

The reproduced G_i^{ads} and ϕ profiles are used to obtain the ion's concentration profile, which then results in the ion's surface excess. Combining all the individual excesses present leads to the total Gibbs-Marangoni pressure and surface tension gradient, eventually. Before these are calculated, the ion's concentration profile is plotted to see if the behaviour of α and β -ions is modelled correctly (Figure 4.3).

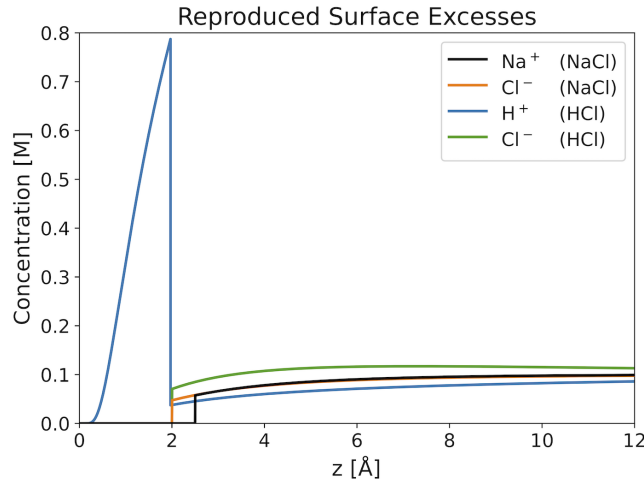


Figure 4.3: Reproduced concentration profiles from Duignan (2021) at a bulk concentration of 0.1 M.

Integrating over these profiles results in $\frac{\Gamma_i}{c}$, which is used to calculate p_{GM} and $\frac{d\gamma}{dc}$. The model also confirmed that these resulting surface excesses fulfilled the electroneutrality condition before continuing. Comparing the results from this work and Duignan (2021) shows great similarities as outcomes deviate less than 10%. This demonstrates that the model is reproduced successfully (Table 4.1).

Table 4.1: Overview of surface tension gradients, electrostatic potentials and Gibbs-Marangoni pressures obtained from Duignan (2021) and this work.

		$\frac{d\gamma}{dc}$ [mN m ⁻¹ M ⁻¹]		$\phi(0)$ [mV]		p_{GM} [Pa]	
		Duignan	Model	Duignan	Model	Duignan	Model
NaCl	($\alpha\alpha$)	1.7	1.72	-20	-18.78	2400	2383.16
NaClO ₄	($\alpha\beta$)	0.6	0.62	-270	-265.90	300	311.73
HCl	($\beta\alpha$)	-0.2	-0.19	400	400.88	30	28.83
HClO ₄	($\beta\beta$)	-2.1	-2.08	150	154.00	3500	3483.93
NaClO ₄ + HCl		-0.2	-0.20	90	93.07	3100	3123.36

Now that the model shows to work as desired, it can be used to see if it can actually be used to describe bubble coalescence inhibition. However, before this can be done, experimental data is needed.

4.2 Experiments

Salts are added to the bubble column to measure how bubble sizes are evolving. However, to make sure that the change in bubble sizes is indeed due to the salts added, the behaviour of the column itself is studied first. This is done in a “dry run”, where the bubble sizes and velocities are measured when changing the gas flow rate in solely water.

4.2.1 Effect of Gas Flow

The dry run is performed by varying the gas flow rate from 10-70 L/min (Figure 4.4). Higher rates were not possible due to the increasing water height, which would eventually cause spillage. From the tested flows, this dry run shows that the measured bubble velocity rises when the gas flow increases. It also seems that the velocity flattens out at higher rates, but no statements can be made from the large interquartile range at these flows. In contrast to the velocity, the bubble size stays relatively constant over the airflow rate. This shows that the formation of bigger bubbles is not restricted by limiting the flow rate to 20 L/min (=1.89 cm/s) for further experiments.

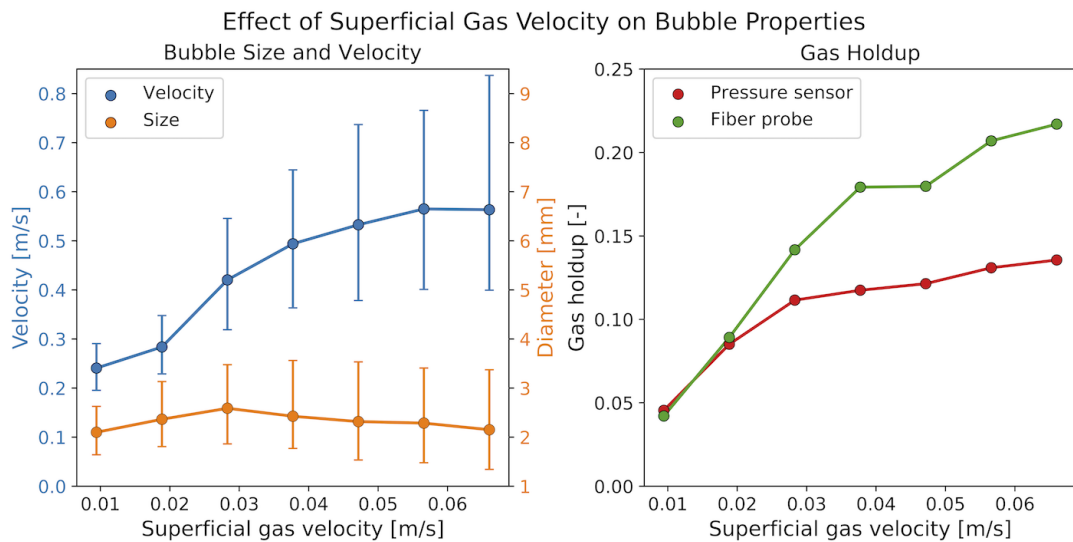
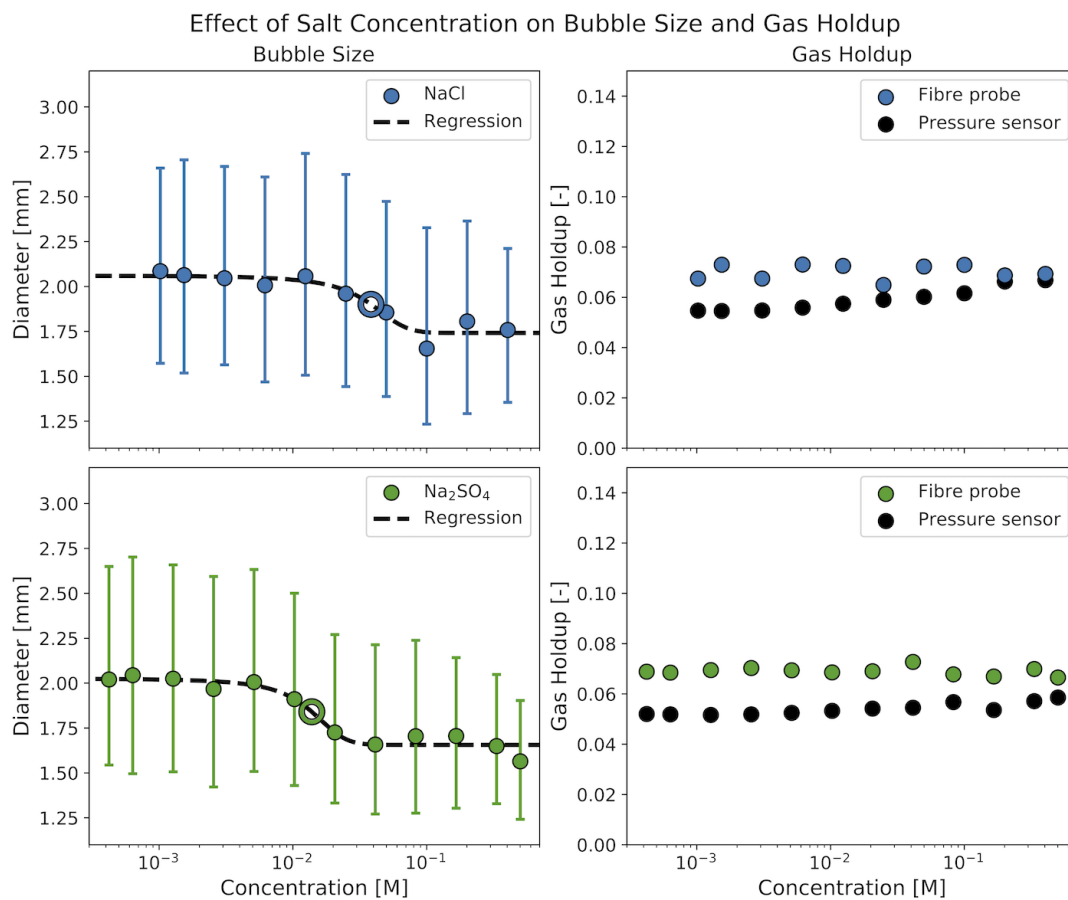


Figure 4.4: Effect of gas flow rate, the superficial gas velocity, on bubble size and velocity (left) and gas holdup (right) in water. Sizes and velocities are represented by the measurement's median and interquartile range.

Looking at the holdup profiles in Figure 4.4 (right), the pressure sensor's measurements deviate from the fibre probe as the superficial gas velocity increases. This is because the fibre probe only measures bubbles at the centre of the column, whereas the pressure sensor considers the entire cross-sectional area. However, despite their differences, similar trends are observed in literature when looking at these profiles (Steynberg et al., 2004) (Manjrekar and Dudukovic, 2019). These trends show how different flow regimes can be identified from the non-linear increase in gas holdup. The static flow pattern mentioned in the Materials & Methods already causes the holdup to be different at the centre and walls of the column. However, this difference is enlarged as the flow regime shifts from more homogeneous to heterogeneous (Esmaili et al., 2015).

4.2.2 Effect of Salts

The preliminary test showed that the gas flow rate of 20 L/min does not limit the maximum bubble size. Therefore when experimenting with different salts, the data point at this concentration can be used as a baseline measurement to compare different results. In this way, the measurements can be assessed whether the results are a good representation of bubble coalescence inhibition. The bubble size has been measured at salt concentrations ranging from 0.0-0.5 M. Moreover, a logistic regression has been made from these results to represent the change in bubble size. Despite the large data distribution, an overall decrease in bubble size is still observed for all salts (Figure 4.5). It needs to be noted that different NH_4Cl batches have been tested with another fibre probe. The reason is that original batches from LabDiscounter disturbed the probe's signal due to the opaqueness it caused when solubilized (Appendix F). NH_4Cl from Thermo Scientific (TS) and Carl Roth (CR) is used as these batches did not interfere with the signal.



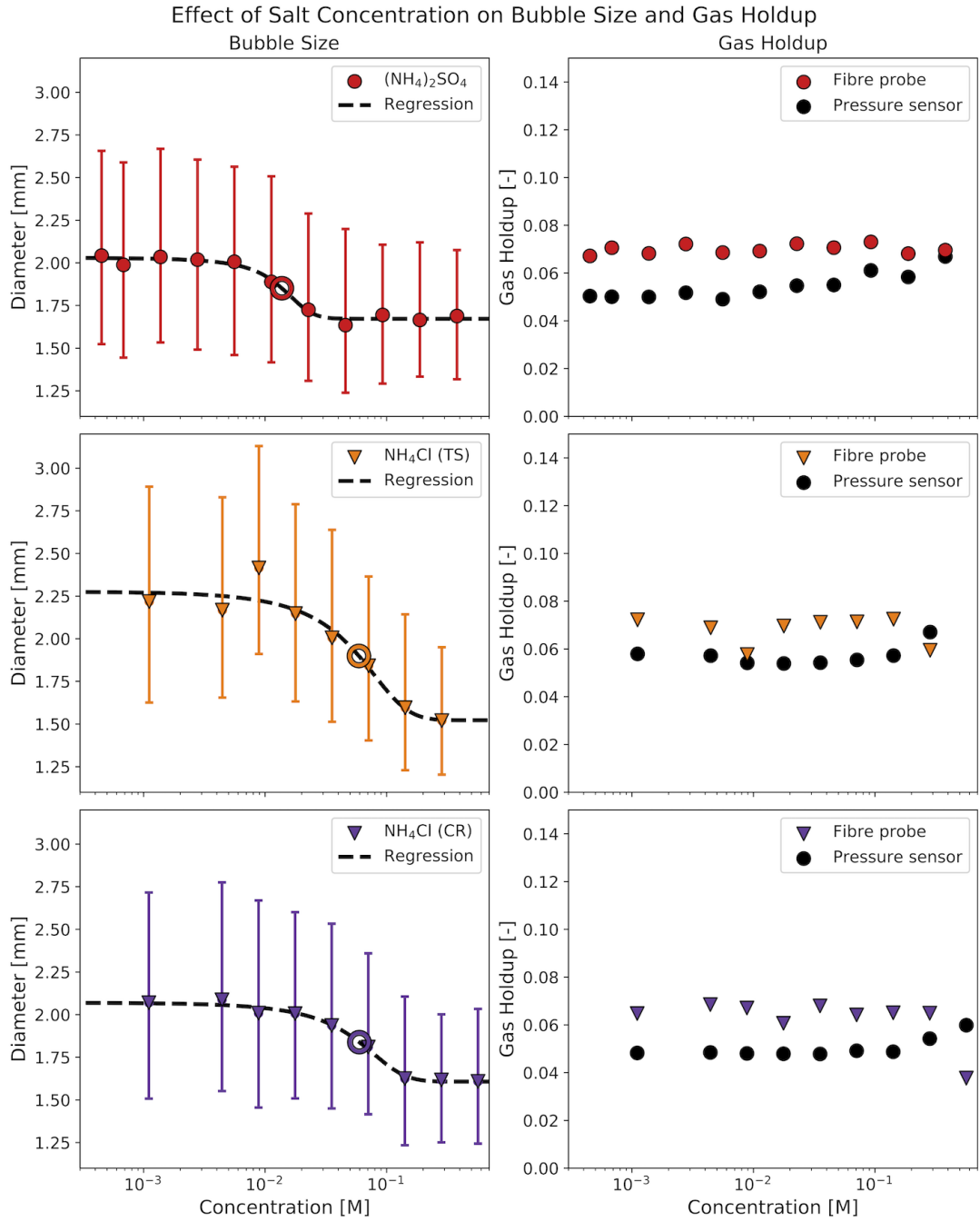


Figure 4.5: Effect of salt concentration on median bubble size and interquartile range (left) and mean gas holdup (right). The open circle depicts the transition point, derived from the regression curve. NH₄Cl's distinct marker represents the different fibre probe used.

Transition concentration

From the logistic regressions in Figure 4.5, three different regimes can be identified. The first regime (i.) is the phase where the salt concentration does not influence the bubble size. This means that bubble sizes stay the same compared to the baseline measurement. At high concentrations, the final regime (iii.), the bubble size is also not influenced by the salt anymore. Both phases are represented by flat regression lines. However, a change in bubble size is happening between the first and final situation. Here, the salt concentration is sufficient to induce bubble coalescence inhibition. This transition regime (ii.) is represented by an S-curve where the measured bubble size shows a steep decrease. This transition phase can also be represented as a single number, the transition concentration (c_t). This is the salt concentration where the measured bubble size is between its initial and final diameter. Different definitions are used in literature to represent this concentration. Some publications define the transition concentration as the point where bubble coalescence is inhibited by 95%, whereas others use 75% or 50%. This inconsistency, together with different experimental conditions and measuring techniques, results in different transition concentrations for the same salt (Firouzi et al., 2015). As there is no set definition, this work opts to use the point of steepest descent, the 50% mark. Part of this reason is that this mark also provides more literature data to compare with.

Comparing the experimental transition concentration in terms of ionic strength shows that NH_4Cl transitions are close between themselves but dissimilar among others (Table 4.2). This difference can be caused by the other fibre probe used for NH_4Cl measurements. This probe is used as the original did show the potential to measure bubbles at higher NH_4Cl concentrations, but the measurements varied from time to time.

Table 4.2: Overview transition concentrations and ionic strengths obtained from experiments.

	Concentration [mM]	Ionic Strength [mM]
NaCl	38.36	38.36
NH_4Cl (TS)	59.08	59.08
NH_4Cl (CR)	59.49	59.49
Na_2SO_4	13.85	41.54
$(\text{NH}_4)_2\text{SO}_4$	13.74	41.22

Even though NH_4Cl 's transition concentrations are similar, the experimental results differ quite a lot when comparing the two transition graphs. Carl Roth shows a similar baseline compared to other salts, whereas Thermo Scientific exhibits a larger bubble size at the baseline and a lower one at the final salt concentration. This difference is hard to explain, especially since the two NH_4Cl measurements were performed in two consecutive days. Maybe, as the probe has not been used before, putting it into use for the first time resulted in dissimilar bubble sizes for Thermo Scientific.

Looking at the other salts, their transition concentrations are similar in terms of ionic strengths. Unfortunately, comparing their actual concentrations with literature data shows that experimental results deviate more than 168% (Table 4.3). A possible explanation for this difference is hard to give as many factors could influence these results, including the experimental conditions and different measuring techniques used. Nonetheless, similar inhibition curves are seen in the literature. This shows that the experimental results still properly represent bubble coalescence inhibition, only at different concentrations.

Table 4.3: Overview of transition concentration ranges at the 50% mark found in the literature, together with their deviation from experimental results in this work. A comprehensive table of literature data, with sources, can be found in Appendix G.

	Concentration [mM]	Δ [%]
NaCl	78.00 - 778.00	≥ 203.34
NH ₄ Cl (TS)	100.00	169.26
NH ₄ Cl (CR)	100.00	168.10
Na ₂ SO ₄	51.00 - 61.00	≥ 368.23
(NH ₄) ₂ SO ₄	31.00	225.62

Gas holdup

The gas holdup profile from the fibre probe stays relatively constant as the salt concentration increases (Figure 4.5). These measurements can deviate a bit between different concentrations due to the gas flow oscillations in the column. Ideally, multiple measurements for a longer time are performed to provide a good statistical representation of this hydrodynamic parameter (Esmaeili et al., 2016). The gas holdup measured by the pressure sensor increases over the concentration, up to the point where the local and global gas holdup measurements are almost similar. This can be explained as the salt, resulting in smaller bubbles, has two effects on the holdup. First, as smaller bubbles are formed, gas rises through the liquid slower, increasing the holdup. The pressure sensor measures this increase. Secondly, as the probe's holdup stays constant, the flow pattern becomes more homogeneous. This results in fewer deviations between the pressure sensor and the fibre probe.

However, the pressure probe's holdup profile slightly differs between different measurements. This is because the column has a small leakage on one of the ports. Therefore, the measured liquid height may be lower than anticipated, which results in a miscalculation of the gas holdup. This has been corrected by taking the voltage difference between the first two measurements when the column contains little to no salt (0.0 & $2.0 \cdot 10^{-3}$ M). This voltage shows how much liquid is lost over a certain time interval, which is included in the calculations to obtain a correct liquid height and gas holdup. Besides leakage, the density and/or height changes due to the addition of salts. This causes the pressure sensor to log a higher voltage. This is corrected by taking the voltage difference between the final two measurements when the water contains the most salt (0.25 & 0.5 M), while also correcting for the previously described leakage. Unfortunately, due to time constraints, it was not manageable to accurately correct the salt additions based on physical values.

Now that all ion combinations are measured by the fibre probe, their experimental results are combined to perform a single logistic regression (Figure 4.6). This resulted in a transition point at an ionic strength of 47.82 mM. This means that the salt's individual transition concentrations deviate between 15-25% from this number. However, it is also interesting to assess how well the model performs on this experimental data.

4.3 Combining the Model with Experimental Data

To see whether p_{GM} can indeed describe bubble coalescence inhibition, the ionic strengths are used in the model to calculate the corresponding p_{GM} (Figure 4.6). As can be seen, this conversion results in very similar trends. This implies that the model behaves as desired and that p_{GM} can represent bubble coalescence inhibition.

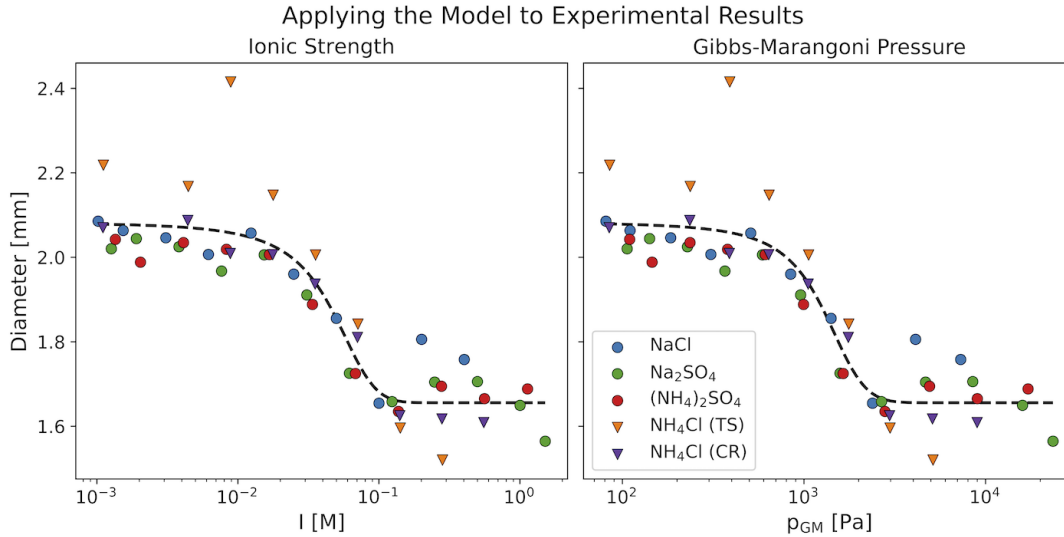


Figure 4.6: Expressing the change in bubble size in terms of the Gibbs-Marangoni pressure.

Similar to the ionic strengths, logistic regression is done on all these data points. This results in an overall transition p_{GM} of 1312.91 Pa. Comparing this number to the individual pressures gives a deviation ranging between 10-22%, which is slightly lower than the deviations found from ionic strengths (Table 4.4). This shows that the p_{GM} cannot only represent bubble coalescence inhibition, but it is also not performing worse compared to the ionic strength.

Table 4.4: Overview of the transition Gibbs-Marangoni pressures.

	p_{GM} [Pa]
NaCl	1121.35
Na ₂ SO ₄	1150.37
(NH ₄) ₂ SO ₄	1178.39
NH ₄ Cl (TS)	1599.28
NH ₄ Cl (CR)	1607.72

However, these p_{GM} values do not necessarily have to mean anything before they are proved to be modelled correctly. Therefore, these results need to be validated. This is done by comparing the accompanied surface tensions with literature data. As the found transition concentrations are in the order of 10^{-2} M, surface tension measurements at these concentrations are elusive. Therefore, the available literature data used for this comparison is composed of NaCl and K₂SO₄ as they represent all the ion valencies used in the experiments (Figure 4.7). Actual values can be found in Appendix H.

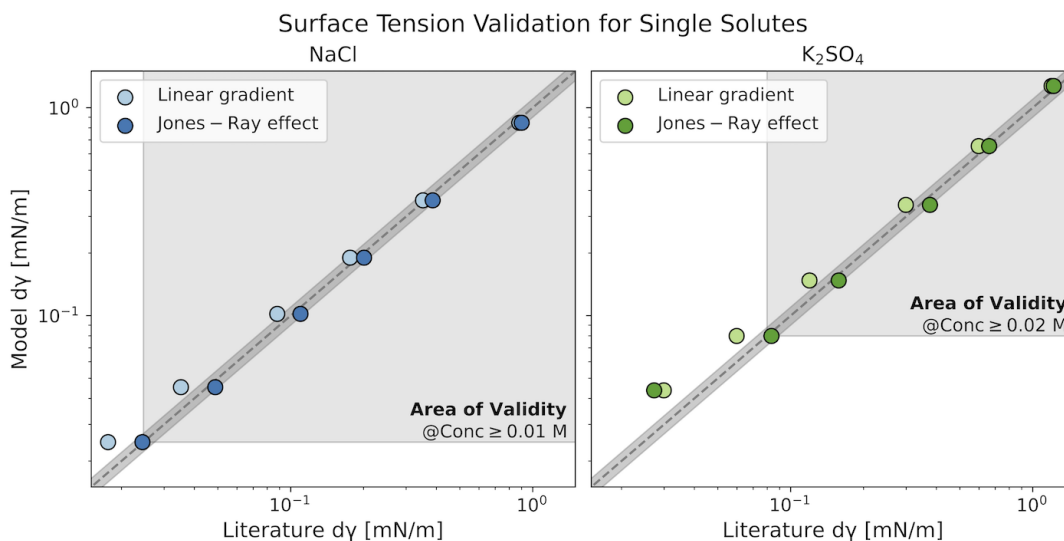


Figure 4.7: Model's surface tensions compared to experimental values from [Henry et al. \(2007\)](#) (linear), [Jones and Ray \(1937\)](#) (non-linear) for K_2SO_4 and [Jones and Ray \(1941\)](#) (non-linear) for NaCl. The dark grey line represents the validity region where surface tensions deviate less than 10% from each other. The area of validity (light grey) implies that deviations are less than 10% from this surface tension onwards.

In Figure 4.7, the p_{GM} is considered valid when the accompanied surface tension deviates less than 10% from literature data. As can be seen, two surface tension data sets are compared with the model's calculation; a linear and non-linear set. The reason for this is that the surface tension gradient is shown to be linear at concentrations of 10^{-1} M and higher ([Henry et al., 2007](#)). However, this appears to be incorrect at lower concentrations ([Jones and Ray, 1937](#)). From this data, it can be seen that the transition p_{GM} can be validated with the non-linear set for the monovalent salts, NaCl and NH_4Cl , as transition concentration is within the area of validity ($c_t \geq 0.01$ M). Moreover, the results remain valid for all larger concentrations measured by [Jones and Ray \(1941\)](#) (Appendix H). As measurements are done up to 2.0 M, this shows a large validity region for monovalent salts.

It appears that the multivalent salts, Na_2SO_4 and $(NH_4)_2SO_4$, cannot be validated at their transition points from both literature values ($c_t \leq 0.02$ M). This shows potential improvements for the model to more accurately calculate p_{GM} and surface tensions at these concentrations. However, also multivalent salts are still valid at the largest concentration measured by [Jones and Ray \(1941\)](#), this time 1.0 M (Appendix H).

Modelling (non-)inhibiting electrolytes

The previous analyses and validations performed are only done with single $\alpha\alpha$ salts. This showed at which concentrations the model can return valid results. However, investigating only these salts does not test the true strength of the model. The model should also be evaluated on α/β combinations and electrolyte mixtures to differentiate itself from the surface tension and ionic strength as bubble coalescence inhibition predictors. To do this, literature data is used as the current experimental setup and surroundings did not allow for testing such electrolytes (Figure 4.8) (Craig et al., 1993) (Henry et al., 2007).

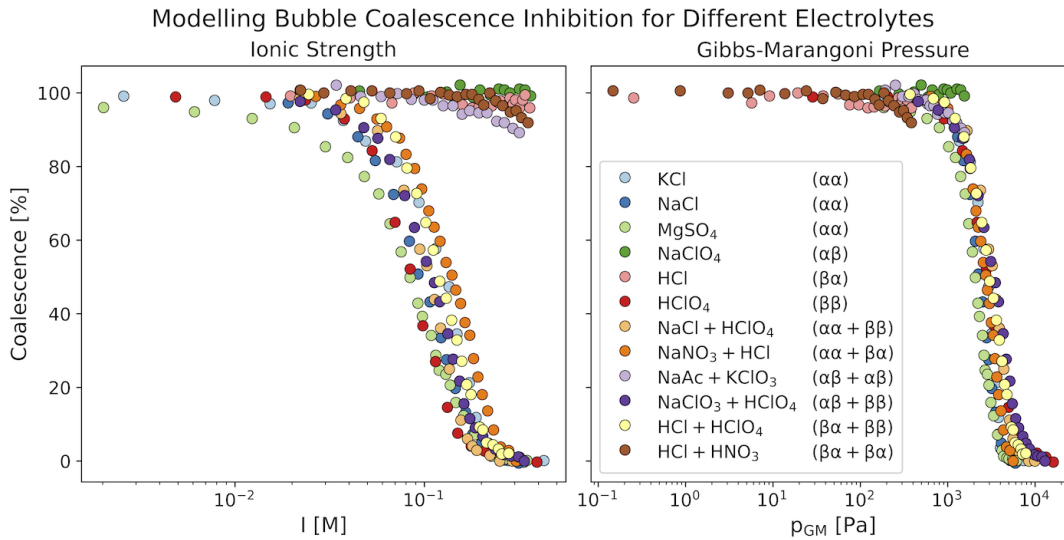


Figure 4.8: Effect of salts on the percentage of bubble coalescence in terms of ionic strength and Gibbs-Marangoni pressure. Data is from Craig et al. (1993) and Henry et al. (2007).

Figure 4.8 visualizes the effect described in the Introduction, where electrolytes do (not) cause bubble coalescence inhibition depending on whether the ions are redistributed along the G/L-interface or not. The ionic strength is shown to be a sufficient predictor as the inhibition curves are relatively similar. However, it fails for electrolytes which do not cause inhibition as these result in (almost) flat lines. Converting all this literature data to p_{GM} does show that all points now fit on a single curve, marking the effectiveness of the model and the importance of considering ion redistribution at the G/L-interface.

It needs to be noted that this literature data cannot be compared with previous experiments directly as a different measuring technique is used. Instead of detecting bubbles with a fibre probe, a laser beam is sent across the column. Depending on the turbidity of the liquid, a photodiode detector logs the remaining intensity on the other side. However, other factors such as opaqueness can also interfere with the laser signal. Moreover, a smaller column and pure N_2 are used (Craig et al., 1993) (Henry et al., 2007).

Nonetheless, these results can still be validated by comparing the calculated surface tensions with literature too (Henry et al., 2007). Instead of pure electrolytes, mixtures are now validated to investigate the wider applicability of the model. This is done by considering two different mixtures; one that is bubble coalescence inhibiting ($\text{NaClO}_3 + \text{HClO}_4$) and one that is not ($\text{NaAc} + \text{KClO}_3$) (Figure 4.9). Actual surface tensions can be found in Appendix H.

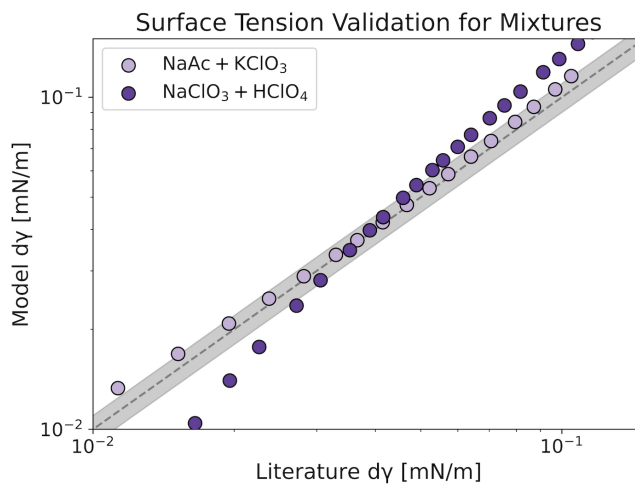


Figure 4.9: Model's surface tensions compared to experimental values from Henry et al. (2007). The $\text{NaClO}_3 + \text{HClO}_4$ mixture originally has a negative surface tension gradient, but its absolute values are plotted as a logarithmic scale is used. The dark grey line represents the validity region where surface tensions deviate less than 10%.

The model's surface tensions for non-inhibiting mixtures ($\text{NaAc} + \text{KClO}_3$) were shown to be close to its literature value. However, this is only for a small concentration range (0.03-0.16 M) as surface tension starts to deviate at higher concentrations. Inhibiting mixtures ($\text{NaClO}_3 + \text{HClO}_4$) show more deviation. The validity interval is even more narrow (0.04-0.07 M). Even though these surface tensions are plotted as their absolute values, they are in fact negative for all inhibiting mixtures. A possible reason for these deviating surface tensions is that the model has difficulties calculating negative values. Also, as surface tension gradients are smaller for mixtures than for pure electrolytes, a small inaccuracy in the model could lead to bigger deviations compared to literature values. Moreover, surface tension measurements of electrolyte mixtures in literature are scarce. This makes it difficult to accurately validate the mixtures.

Non-inhibiting electrolytes at high concentrations

Even though the literature data from Figure 4.8 states that some electrolytes do not inhibit bubble coalescence, a small decrease in coalescence percentage is seen at the last measurements of these compounds. This raises the curiosity of whether this statement is actually true or not. Therefore, the effect of these non-inhibiting electrolytes at high ionic strengths (≥ 0.5 M) is modelled too. Unfortunately, only one study regarding this phenomenon is found (Figure 4.10) (Christenson et al., 2008). Also here, it needs to be noted that another different measuring technique is used compared to previous data. In Christenson et al. (2008), measurements are not performed on bubble swarms. Instead, these experiments were done by bringing two single bubbles together and studying whether they merge or not. This data can therefore not be directly compared with previous results.

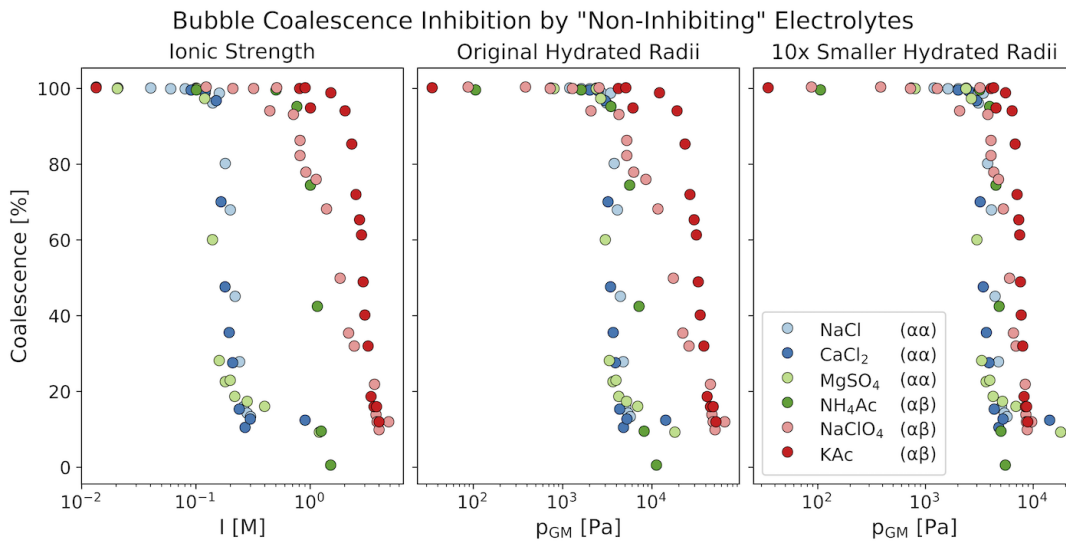


Figure 4.10: Effect of “non-inhibiting” electrolytes on the percentage of bubble coalescence in terms of ionic strength and Gibbs-Marangoni pressure. Hydrated radii of ions are adjusted to obtain less spreading of Gibbs-Marangoni pressures. Data obtained from Christenson et al. (2008).

Figure 4.10 shows that “non-inhibiting” electrolytes do indeed cause bubble coalescence inhibition at higher ionic strengths. However, the resulting transition concentrations are more dispersed compared to “inhibiting” salts. A possible explanation for this spread is that these high concentrations affect liquid properties, such as viscosity. Furthermore, the measurements were performed with salts of analytical grade (purity $\geq 95\%$) (Christenson et al., 2008). The accompanied impurities could therefore have an additional contribution to bubble coalescence inhibition at these higher concentrations. Unfortunately, additional surface tension measurements were not performed to study if this had an influence. In the end, many factors could have affected the final measurements.

The data from [Christenson et al. \(2008\)](#) is tested on the model to see whether these dispersed “non-inhibiting” electrolytes measurements would still result in similar p_{GM} values compared to the α salts. When using the same parameters as previously used, the calculated pressures do cause the inhibition curve to be more narrow compared to the ionic strengths. However, this spread is not as narrow as the results from previous literature data (Figure 4.8). As the p_{GM} from “non-inhibiting” electrolytes is distinctively different from α salts, this shows that (i.) the model is not accurate anymore or (ii.) physical conditions change at these high concentrations. If the model is inaccurate, this shows its applicability limitations. If there is a potential physical difference, attempts can be made to resolve this problem. The latter is done by changing the hydrated radius at higher concentrations. At these concentrations, it could happen that there are not enough water molecules available for an ion to reach its maximum hydrated radius. To test this, the hydrated radius of ions is changed by a factor 10^{-1} when the concentrations exceed 0.5 M. This eventually does result in a more narrow inhibition curve (Figure 4.10). To check whether changing the hydrated radii is justifiable, the model’s surface tensions are compared to literature, again (Figure 4.11) ([Henry et al., 2007](#)). These values can be found in Appendix H.

As seen in Figure 4.11, changing the hydrated radii results in more surface tension deviation. This implies that even though the p_{GM} spread becomes more narrow, the results are becoming less valid. Figure 4.11 also shows that the model has its general limitations at concentrations above 1.5 M, as this is outside the area of validity. It is also not unreasonable that validity stops at concentrations above 1.5 M. This is because the electrostatic effect is overshadowed by other factors such as ion polarizability, solvation energy and ion-charge density. In fact, these contributions are already important to take into account at concentrations in the order of 10^{-2} M ([Bera, 2016](#)). Unfortunately, as opposed to the maximum validity, its minimum could not be analyzed for KAc. The reason is that [Christenson et al. \(2008\)](#) did not perform sufficient measurements at lower concentrations (Appendix H).

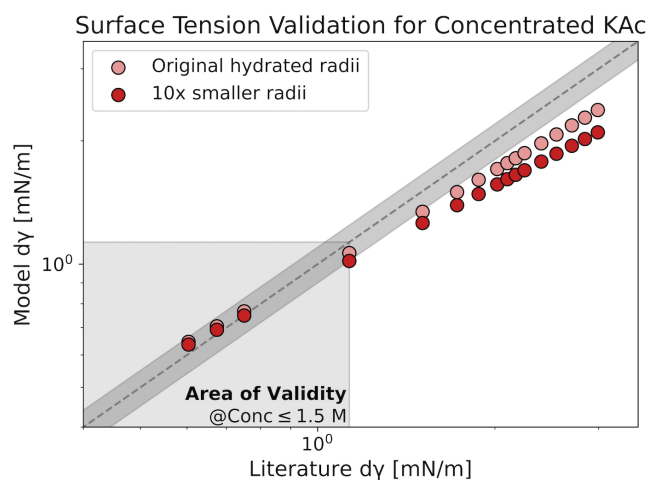


Figure 4.11: Model’s surface tensions compared to experimental values from [Henry et al. \(2007\)](#). Area of validity implies a model’s deviation of less than 10% with literature.

Looking back at all pure electrolytes, large validity ranges are found to where this model is accurately applicable (Table 4.5). Due to these high concentrations ≥ 1.0 M, this model is always applicable within biological limits. However, these validity ranges are significantly shorter when mixtures are involved. As mentioned before, reasons for this could be the small surface tension gradients involved, or the limited/inaccurate literature data. Therefore, it may be arguable that mixture results can be valid as long as their individual surface tensions are correct, which gives the same validity ranges as pure electrolytes.

Table 4.5: Validity concentration ranges for different solutes. ⁱhigher concentrations were not tested by Jones and Ray (1937) and Jones and Ray (1941). ⁱⁱlower concentrations could not be validated from Christenson et al. (2008).

Solute	Concentration [M]
Inhibiting monovalent salt	0.01 - 2.0 ⁱ
Inhibiting multivalent salt	0.02 - 1.0 ⁱ
Non-inhibiting monovalent salt	≤ 1.5 ⁱⁱ
Non-inhibiting mixture	0.03 - 0.16
Inhibiting mixture	0.04 - 0.07

5 Conclusion

The [Results & Discussion](#) arose interesting insights regarding the applicability and accuracy of the Gibbs-Marangoni pressure (p_{GM}) to describe bubble coalescence inhibition by salts. Testing this applicability was possible by developing a model which can calculate the p_{GM} by considering the (re)distribution of ions along the G/L-interface. To make sure the model is behaving correctly, its results were compared with [Duignan \(2021\)](#). In fact, this showed that these numbers deviated less than 10% from each other. This underpins that the model is working as desired and that miscalculations of future results can be exempted.

However, to use the model, experiments were performed to measure the effect of salt on gas bubble sizes. This showed that all salts (NaCl, NH₄Cl, Na₂SO₄ and (NH₄)₂SO₄) do cause bubble coalescence inhibition and that similar inhibition curves were obtained. However, some differences in bubble sizes were seen as different fibre probes were used. Moreover, a single measurement itself also showed large bubble size distributions. Nonetheless, the found transition concentrations deviate less than 25% from each other. So, the experiments do describe bubble coalescence inhibition, but the large data distribution and different probes being used do take away some accuracy of these measurements. Additionally, these concentrations deviate more than 168% of the values found in the literature. An explanation is hard to give as many factors could influence these results, including the experimental conditions and different measuring techniques used.

Applying these experimental results to the model showed that the calculated transition p_{GM} deviated less than 22%. Therefore, the model and p_{GM} are not performing worse in representing bubble coalescence inhibition when compared to the transition concentrations from above. Moreover, testing additional non-inhibiting electrolytes (mixtures) showed that the model can also explain their non-inhibiting feature. This is because the resulting p_{GM} is lower than for inhibiting electrolytes, therefore not reaching the threshold p_{GM} to inhibit coalescence. However, non-inhibiting electrolytes could still get over this value at sufficient concentrations. The model can represent even this, but requires some parameters (ionic hydrated radii) to decrease.

To make sure that the calculated p_{GM} is true and not a made-up number, all results are validated by comparing the additionally calculated surface tensions with the literature. If the model's surface tension deviates less than 10%, the p_{GM} is considered valid. These analyses showed that pure electrolytes can be accurately modelled in a concentration range of around 0.02-1.50 M. However, mixtures show a significantly smaller validity region, 0.03-0.16 M at best. From all these findings, the main research question can be answered:

Considering ion redistribution along the G/L-interface due to electrostatic potential, does it contribute to accurately predicting bubble coalescence inhibition for salts?

Yes, this mechanism can contribute to predicting bubble coalescence inhibition for salts as it shows more consistency compared to the surface tension and ionic strength. This is because all electrolytes can be represented in terms of p_{GM} and analyzed if this pressure is sufficient for bubble coalescence inhibition to happen. However, the model's accuracy is debatable as results, especially mixtures, cannot always be validated.

5.1 Recommendations

To better validate the model, more and different experiments can be performed. Moreover, some adjustments or additions to the model may be useful for use in future bubble column simulations.

5.1.1 Experiments

Even though the experimental setup used suffices for the experiments, (i.) a wider column, (ii.) a higher measuring height and (iii.) a better sparger setup would be ideal for bubble size measurements. A wider column and larger gas box under the sparger will lead to a more homogeneous flow of bubbles in the liquid. This means that bubbles will rise more equally through the liquid. Therefore, no/fewer differences in results will be seen when measuring at the centre or near the wall. A higher measuring height gives the bubbles more time to interact with each other, making sure that bubbles reach their maximum achievable size. This allows doing fibre probe measurements with smaller bubble size distributions.

Moreover, testing more salt (mixtures) with the fibre probe helps to understand if the model is still applicable to these results. Measurements can also be extended to (non-)inhibiting mixtures and even other types of compounds, such as acids.

Furthermore, as surface tension data for electrolyte mixtures is scarce, the measuring can be performed to validate the model with. Maybe it is possible to better validate the model in the future.

5.1.2 Model

To have a more valid model, the addition of other factors such as ion polarizability, solvation energy and ion-charge density can contribute to more accurate results. However, this will increase the complexity of the model. As the current model already takes some seconds to calculate, it may be beneficial to first make it more time-efficient.

Also, the model can be generalised by applying it to different compounds, such as acids. By expanding this model, it is hopefully possible to take every compound of a fermentation broth into account. This will make bubble column simulation more realistic and accurate.



Bibliography

- María Eugenia Aguilera, Antonieta Ojeda, Carolina Rondón, and Aura López De Ramos. Effect of Electrolytes on Bubble Coalescence in Columns Observed with Visualization Techniques. *Annals of the New York Academy of Sciences*, 972(1):242–246, 2002. ISSN 1749-6632. doi:[10.1111/j.1749-6632.2002.tb04579.x](https://doi.org/10.1111/j.1749-6632.2002.tb04579.x).
- Zahra Bahri, Sied Ziaedin Shafaei, and Mohammad Karamoozian. Investigation of Effective Parameters on the Gas Holdup in Column Flotation of a Coal Tailing Sample. *International Journal of Coal Preparation and Utilization*, 33(2):47–58, March 2013. ISSN 1939-2699. doi:[10.1080/19392699.2012.759944](https://doi.org/10.1080/19392699.2012.759944).
- Bijoyendra Bera. *Ion and surfactant induced wetting transition*. PhD, University of Twente, Enschede, The Netherlands, February 2016. ISBN: 9789036540490.
- M. R. Bhole, J. B. Joshi, and D. Ramkrishna. CFD simulation of bubble columns incorporating population balance modeling. *Chemical Engineering Science*, 63(8):2267–2282, April 2008. ISSN 0009-2509. doi:[10.1016/j.ces.2008.01.013](https://doi.org/10.1016/j.ces.2008.01.013).
- H. K. Christenson, R. E. Bowen, J. A. Carlton, J. R. M. Denne, and Y. Lu. Electrolytes that Show a Transition to Bubble Coalescence Inhibition at High Concentrations. *The Journal of Physical Chemistry C*, 112(3):794–796, January 2008. ISSN 1932-7447. doi:[10.1021/jp075440s](https://doi.org/10.1021/jp075440s). Publisher: American Chemical Society.
- V. S. J. Craig, B. W. Ninham, and R. M. Pashley. Effect of electrolytes on bubble coalescence. *Nature*, 364(6435):317–319, July 1993. ISSN 1476-4687. doi:[10.1038/364317a0](https://doi.org/10.1038/364317a0). Publisher: Nature Publishing Group.
- Alexandre P. dos Santos and Yan Levin. Surface tensions and surface potentials of acid solutions. *The Journal of Chemical Physics*, 133(15):154107, October 2010. ISSN 0021-9606. doi:[10.1063/1.3505314](https://doi.org/10.1063/1.3505314).
- Alexandre P. dos Santos, Alexandre Diehl, and Yan Levin. Surface Tensions, Surface Potentials, and the Hofmeister Series of Electrolyte Solutions. *Langmuir*, 26(13):10778–10783, July 2010. ISSN 0743-7463. doi:[10.1021/la100604k](https://doi.org/10.1021/la100604k). Publisher: American Chemical Society.
- GEORGE DROGARIS. Studies of Coalescence of Bubble Pairs. *Chemical Engineering Communications*, 23(1-3):11–26, October 1983. ISSN 0098-6445. doi:[10.1080/00986448308940461](https://doi.org/10.1080/00986448308940461).
- Timothy T. Duignan. The surface potential explains ion specific bubble coalescence inhibition. *Journal of Colloid and Interface Science*, 600:338–343, October 2021. ISSN 0021-9797. doi:[10.1016/j.jcis.2021.04.144](https://doi.org/10.1016/j.jcis.2021.04.144).
- Timothy T. Duignan, Mengsu Peng, Anh V. Nguyen, X. S. Zhao, Marcel D. Baer, and Christopher J. Mundy. Detecting the undetectable: The role of trace surfactant in the Jones-Ray effect. *The Journal of Chemical Physics*, 149(19):194702, November 2018. ISSN 0021-9606. doi:[10.1063/1.5050421](https://doi.org/10.1063/1.5050421).

Bibliography

- Amin Esmaeili, Christophe Guy, and Jamal Chaouki. The effects of liquid phase rheology on the hydrodynamics of a gas–liquid bubble column reactor. *Chemical Engineering Science*, 129:193–207, June 2015. ISSN 0009-2509. doi:[10.1016/j.ces.2015.01.071](https://doi.org/10.1016/j.ces.2015.01.071).
- Amin Esmaeili, Christophe Guy, and Jamal Chaouki. Local hydrodynamic parameters of bubble column reactors operating with non-Newtonian liquids: Experiments and models development. *AIChE Journal*, 62(4):1382–1396, 2016. ISSN 1547-5905. doi:[10.1002/aic.15130](https://doi.org/10.1002/aic.15130).
- Mahshid Firouzi. Effects of monovalent anions and cations on drainage and lifetime of foam films at different interface approach speeds. *Advanced Powder Technology*, 25(4):1212–1219, July 2014. ISSN 0921-8831. doi:[10.1016/j.appt.2014.06.004](https://doi.org/10.1016/j.appt.2014.06.004).
- Mahshid Firouzi, Tony Howes, and Anh V. Nguyen. A quantitative review of the transition salt concentration for inhibiting bubble coalescence. *Advances in Colloid and Interface Science*, 222:305–318, August 2015. ISSN 0001-8686. doi:[10.1016/j.cis.2014.07.005](https://doi.org/10.1016/j.cis.2014.07.005).
- Kasimir P. Gregory, Gareth R. Elliott, Hayden Robertson, Anand Kumar, Erica J. Wanless, Grant B. Webber, Vincent S. J. Craig, Gunther G. Andersson, and Alister J. Page. Understanding specific ion effects and the Hofmeister series. *Physical Chemistry Chemical Physics*, 24(21):12682–12718, 2022. ISSN 1463-9076, 1463-9084. doi:[10.1039/D2CP00847E](https://doi.org/10.1039/D2CP00847E).
- J. J. Heijnen and K. Van't Riet. Mass transfer, mixing and heat transfer phenomena in low viscosity bubble column reactors. *The Chemical Engineering Journal*, 28(2):B21–B42, April 1984. ISSN 0300-9467. doi:[10.1016/0300-9467\(84\)85025-X](https://doi.org/10.1016/0300-9467(84)85025-X).
- Christine L. Henry, Casuarina N. Dalton, Lehoa Scruton, and Vincent S. J. Craig. Ion-Specific Coalescence of Bubbles in Mixed Electrolyte Solutions. *The Journal of Physical Chemistry C*, 111(2):1015–1023, January 2007. ISSN 1932-7447. doi:[10.1021/jp066400b](https://doi.org/10.1021/jp066400b). Publisher: American Chemical Society.
- B. G. Hermann, K. Blok, and M. K. Patel. Producing Bio-Based Bulk Chemicals Using Industrial Biotechnology Saves Energy and Combats Climate Change. *Environmental Science & Technology*, 41(22):7915–7921, November 2007. ISSN 0013-936X. doi:[10.1021/es062559q](https://doi.org/10.1021/es062559q). Publisher: American Chemical Society.
- Grinnell Jones and Wendell A. Ray. The Surface Tension of Solutions of Electrolytes as a Function of the Concentration. I. A Differential Method for Measuring Relative Surface Tension. *Journal of the American Chemical Society*, 59(1):187–198, January 1937. ISSN 0002-7863. doi:[10.1021/ja01280a048](https://doi.org/10.1021/ja01280a048). Publisher: American Chemical Society.
- Grinnell Jones and Wendell A. Ray. The Surface Tension of Solutions of Electrolytes as a Function of the Concentration. III. Sodium Chloride. *Journal of the American Chemical Society*, 63(12):3262–3263, December 1941. ISSN 0002-7863. doi:[10.1021/ja01857a007](https://doi.org/10.1021/ja01857a007). Publisher: American Chemical Society.
- Stoyan I. Karakashev, Phong T. Nguyen, Roumen Tsekov, Marc A. Hampton, and Anh V. Nguyen. Anomalous Ion Effects on Rupture and Lifetime of Aqueous Foam Films Formed from Monovalent Salt Solutions up to Saturation Concentration. *Langmuir*, 24(20):11587–11591, October 2008. ISSN 0743-7463. doi:[10.1021/la801456j](https://doi.org/10.1021/la801456j). Publisher: American Chemical Society.
- Michael Köpke and Séan D Simpson. Pollution to products: recycling of ‘above ground’ carbon by gas fermentation. *Current Opinion in Biotechnology*, 65:180–189, October 2020. ISSN 0958-1669. doi:[10.1016/j.copbio.2020.02.017](https://doi.org/10.1016/j.copbio.2020.02.017).

- Anthony Lefebvre, Yann Mezui, Martin Obligado, Stéphane Gluck, and Alain Cartel-lier. A new, optimized Doppler optical probe for phase detection, bubble velocity and size measurements: Investigation of a bubble column operated in the heterogeneous regime. *Chemical Engineering Science*, 250:117359, March 2022. ISSN 0009-2509. doi:[10.1016/j.ces.2021.117359](https://doi.org/10.1016/j.ces.2021.117359).
- C. Leonard, J. H. Ferrasse, O. Boutin, S. Lefevre, and A. Viand. Bubble column reactors for high pressures and high temperatures operation. *Chemical Engineering Research and Design*, 100:391–421, August 2015. ISSN 0263-8762. doi:[10.1016/j.cherd.2015.05.013](https://doi.org/10.1016/j.cherd.2015.05.013).
- Richard R. Lessard. Bubble Coalescence and Gas Transfer in Aqueous Electrolytic Solutions. *Industrial & Engineering Chemistry Fundamentals*, 10(2):260–269, May 1971. ISSN 0196-4313. doi:[10.1021/i160038a012](https://doi.org/10.1021/i160038a012). Publisher: American Chemical Society.
- Yan Levin, Alexandre P. dos Santos, and Alexandre Diehl. Ions at the Air-Water Interface: An End to a Hundred-Year-Old Mystery? *Physical Review Letters*, 103(25):257802, December 2009. doi:[10.1103/PhysRevLett.103.257802](https://doi.org/10.1103/PhysRevLett.103.257802). Publisher: American Physical Society.
- Bo Liu, Rogerio Manica, Zhenghe Xu, and Qingxia Liu. Ion specificity modulated inhomogeneous interfacial flow inhibits bubble coalescence in electrolyte solutions. *Physical Review Letters*, 131(10):104003, September 2023. ISSN 0031-9007, 1079-7114. doi:[10.1103/PhysRevLett.131.104003](https://doi.org/10.1103/PhysRevLett.131.104003). arXiv:2007.10972 [cond-mat, physics:physics].
- Onkar N. Manjrekar and Milorad P. Dudukovic. Identification of flow regime in a bubble column reactor with a combination of optical probe data and machine learning technique. *Chemical Engineering Science: X*, 2:100023, May 2019. ISSN 2590-1400. doi:[10.1016/j.cesx.2019.100023](https://doi.org/10.1016/j.cesx.2019.100023).
- G. Marrucci. A theory of coalescence. *Chemical Engineering Science*, 24(6):975–985, June 1969. ISSN 0009-2509. doi:[10.1016/0009-2509\(69\)87006-5](https://doi.org/10.1016/0009-2509(69)87006-5).
- Dale D. McClure, Hannah Norris, John M. Kavanagh, David F. Fletcher, and Geoffrey W. Barton. Towards a CFD model of bubble columns containing significant surfactant levels. *Chemical Engineering Science*, 127:189–201, May 2015. ISSN 0009-2509. doi:[10.1016/j.ces.2015.01.025](https://doi.org/10.1016/j.ces.2015.01.025).
- Vincent Ngu, Jérôme Morchain, and Arnaud Cockx. Spatio-temporal 1D gas–liquid model for biological methanation in lab scale and industrial bubble column. *Chemical Engineering Science*, 251:117478, April 2022. ISSN 0009-2509. doi:[10.1016/j.ces.2022.117478](https://doi.org/10.1016/j.ces.2022.117478).
- Phong T. Nguyen, Marc A. Hampton, Anh V. Nguyen, and Greg R. Birkett. The influence of gas velocity, salt type and concentration on transition concentration for bubble coalescence inhibition and gas holdup. *Chemical Engineering Research and Design*, 90(1):33–39, January 2012. ISSN 0263-8762. doi:[10.1016/j.cherd.2011.08.015](https://doi.org/10.1016/j.cherd.2011.08.015).
- Lars Puiman, Britt Abrahamson, Rob G. J. M. van der Lans, Cees Haringa, Henk J. Noorman, and Cristian Picioreanu. Alleviating mass transfer limitations in industrial external-loop syngas-to-ethanol fermentation. *Chemical Engineering Science*, 259:117770, September 2022. ISSN 0009-2509. doi:[10.1016/j.ces.2022.117770](https://doi.org/10.1016/j.ces.2022.117770).
- J. J. Quinn, J. M. Sovechles, J. A. Finch, and K. E. Waters. Critical coalescence concentration of inorganic salt solutions. *Minerals Engineering*, 58:1–6, April 2014. ISSN 0892-6875. doi:[10.1016/j.mineng.2013.12.021](https://doi.org/10.1016/j.mineng.2013.12.021).

Bibliography

- Jarl B. Rosenholm. Critical evaluation of dipolar, acid-base and charge interactions I. Electron displacement within and between molecules, liquids and semiconductors. *Advances in Colloid and Interface Science*, 247:264–304, September 2017. ISSN 0001-8686. doi:[10.1016/j.cis.2017.06.004](https://doi.org/10.1016/j.cis.2017.06.004).
- Kristin L. Sainani. Dealing With Non-normal Data. *PM&R*, 4(12):1001–1005, 2012. ISSN 1934-1563. doi:[10.1016/j.pmrj.2012.10.013](https://doi.org/10.1016/j.pmrj.2012.10.013).
- A. P. Steynberg, M. E. Dry, B. H. Davis, and B. B. Breman. Chapter 2 - Fischer-Tropsch Reactors. In André Steynberg and Mark Dry, editors, *Studies in Surface Science and Catalysis*, volume 152 of *Fischer-Tropsch Technology*, pages 64–195. Elsevier, January 2004. doi:[10.1016/S0167-2991\(04\)80459-2](https://doi.org/10.1016/S0167-2991(04)80459-2).
- I. Katharina Stoll, Nikolaos Boukis, and Jörg Sauer. Syngas Fermentation to Alcohols: Reactor Technology and Application Perspective. *Chemie Ingenieur Technik*, 92(1-2):125–136, 2020. ISSN 1522-2640. doi:[10.1002/cite.201900118](https://doi.org/10.1002/cite.201900118).
- Ajay Sujan and Raj K. Vyas. Estimation of transition concentration of aqueous mixtures of single and binary electrolytes for bubble coalescence inhibition. *Chemical Papers*, 72(10):2539–2559, October 2018. ISSN 1336-9075. doi:[10.1007/s11696-018-0470-2](https://doi.org/10.1007/s11696-018-0470-2).
- Mauro Torli, Luydmila Geer, Georgios M. Kontogeorgis, and Philip L. Fosbøl. Solubility of Syngas Components in Water, Acetic Acid, and Alcohol Using New Standard Fugacity Methodology. *Industrial & Engineering Chemistry Research*, 57(49):16958–16977, December 2018. ISSN 0888-5885. doi:[10.1021/acs.iecr.8b03954](https://doi.org/10.1021/acs.iecr.8b03954). Publisher: American Chemical Society.
- Yuki Uematsu, Douwe Jan Bonthuis, and Roland R. Netz. Charged Surface-Active Impurities at Nanomolar Concentration Induce Jones–Ray Effect. *The Journal of Physical Chemistry Letters*, 9(1):189–193, January 2018. doi:[10.1021/acs.jpcl.7b02960](https://doi.org/10.1021/acs.jpcl.7b02960). Publisher: American Chemical Society.
- Jille van der Bom. *Bubble property determination. Comparison between bubble data from a fibre probe, and a camera*. Bachelor Thesis, Delft University of Technology, Delft, July 2023.
- R. Volger, L. Puiman, and C. Haringa. Bubbles and Broth: A review on the impact of broth composition on bubble column bioreactor hydrodynamics. *Biochemical Engineering Journal*, 201:109124, January 2024. ISSN 1369-703X. doi:[10.1016/j.bej.2023.109124](https://doi.org/10.1016/j.bej.2023.109124).
- J. Zahradnik, M. Fialová, and V. Linek. The effect of surface-active additives on bubble coalescence in aqueous media. *Chemical Engineering Science*, 54(21):4757–4766, November 1999. ISSN 0009-2509. doi:[10.1016/S0009-2509\(99\)00192-X](https://doi.org/10.1016/S0009-2509(99)00192-X).
- Xibao Zhang and Zhenghong Luo. Bubble size modeling approach for the simulation of bubble columns. *Chinese Journal of Chemical Engineering*, 53:194–200, January 2023. ISSN 1004-9541. doi:[10.1016/j.cjche.2022.02.005](https://doi.org/10.1016/j.cjche.2022.02.005).
- Stefan A Zieminski, Robert M Hume, and Robert Durham. Rates of oxygen transfer from air bubbles to aqueous NaCl solutions at various temperatures. *Marine Chemistry*, 4(4):333–346, December 1976. ISSN 0304-4203. doi:[10.1016/0304-4203\(76\)90019-0](https://doi.org/10.1016/0304-4203(76)90019-0).

A Ionic Adsorption-Free Energy

The [Theoretical Background](#) describes that the model allows different adsorption-free energy functions to be used, which is beneficial when having multiple species. The recreated results from [Duignan \(2021\)](#) also utilize different G^{ads} -functions as both α (Na^+ & Cl^-) and β -ions (H^+ & ClO_4^-) are modelled here. These two types of ions have very different behaviour in the liquid ([Duignan, 2021](#)). Therefore, different functions are used for H^+ and ClO_4^- (Equations [A.1](#) & [A.2](#)). Here, the function for ClO_4^- is also the function used to model other β ions.

$$G_H^{ads}(z) = \begin{cases} \frac{1}{4\pi z} \frac{e^2}{4\epsilon_0\epsilon_w} \exp[-2\kappa z], & \text{for } z \geq a_{h,H} \\ \frac{1}{4\pi z} \frac{e^2}{4\epsilon_0\epsilon_w} \exp[-2\kappa z] - 3.05k_B T, & \text{for } 0 < z < a_{h,H} \end{cases} \quad (\text{A.1})$$

$$G_\beta^{ads}(z) = \begin{cases} \frac{W_\beta a_{h,\beta}}{z} \exp[-2\kappa(z - a_{h,\beta})], & \text{for } z \geq a_{h,\beta} \\ \frac{W_\beta a_{h,\beta}}{z} \exp[-2\kappa(z - a_{h,\beta})] - 2.1k_B T, & \text{for } 0 < z < a_{h,\beta} \end{cases} \quad (\text{A.2})$$

Depending on the desired accuracy of results, complex or simplified G^{ads} -functions can be used. A simplified example is the square-well approach (Figure [A.1](#)), where X is a constant energy value within width w (Equation [A.3](#)). This shows that the model's results are indeed affected by the G^{ads} -functions, but they don't play a deciding factor ([Duignan, 2021](#)).

$$G_i^{ads}(z) = \begin{cases} 0, & \text{for } z \geq w \\ Xk_B T, & \text{for } 0 < z < w \end{cases} \quad (\text{A.3})$$

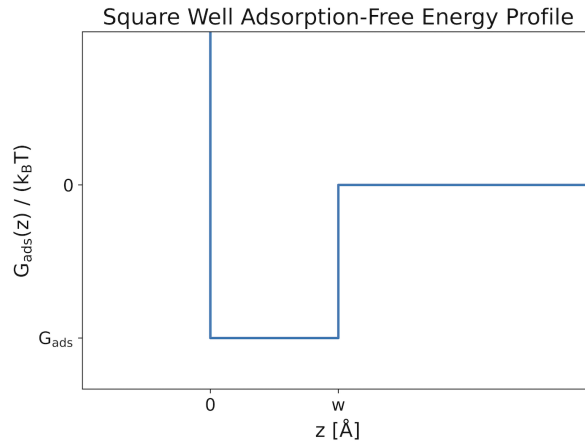


Figure A.1: Schematic representation of a square well adsorption-free energy.

B Pressure Sensor Calibration

As mentioned in the [Theoretical Background](#), the pressure sensor only returns a voltage signal. A way needs to be found to convert this voltage into the corresponding water level in the column. To do this, a calibration line is made (Figure B.1). This is achieved by taking voltage measurements at known water levels. Performing a linear fit results in an equation where the height is a function of the voltage (Equation B.1).

$$H(U) = 7.123 * 10^{-2}U - 1.509 * 10^{-3} \quad (\text{B.1})$$

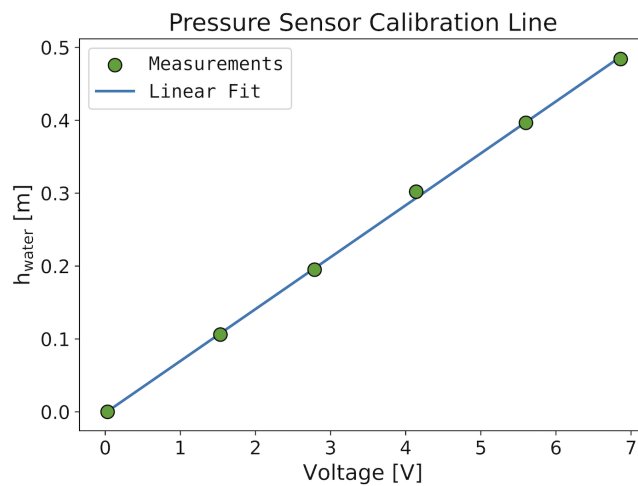


Figure B.1: The pressure sensor's calibration line (blue) is established from the measurements (green). This calibration makes it possible to convert the measured voltage into a water height.

C Bubble Size Distributions

Clear and reliable results are important when studying the influence of salts on bubble coalescence. Therefore, visualisation and analysis of the data need to be done properly. This Appendix describes the logical reasoning behind the data analysis done in this work, specifically focused on bubble size measurements by the optical fibre probe when salt is added. When performing such measurements, the resulting histogram shows the size distribution of all valid bubbles that have been measured (Figure C.1).

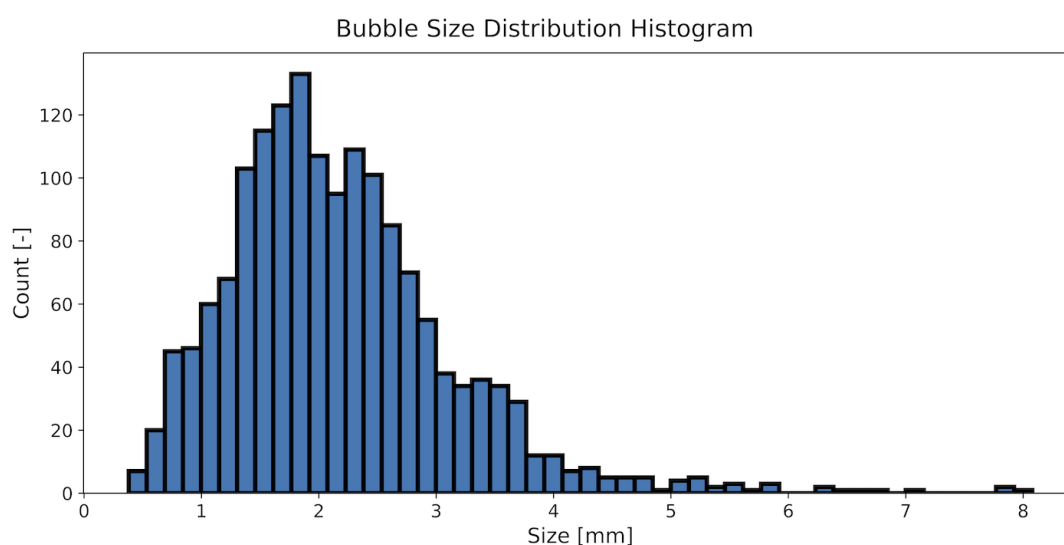


Figure C.1: Histogram of bubble sizes measured by the optical fibre probe.

To show the importance of proper data analysis and visualisation, a set of measurements from $(\text{NH}_4)_2\text{SO}_4$ is used as an example in this Appendix. From Figure C.2, comparing the different measurements is difficult due to the large varieties in measured bubble sizes. Therefore, the data should be represented even more concisely. This is preferably done by representing every histogram as a single point. In data analysis, there are typically two types of values that can be used to achieve this: means or percentiles.

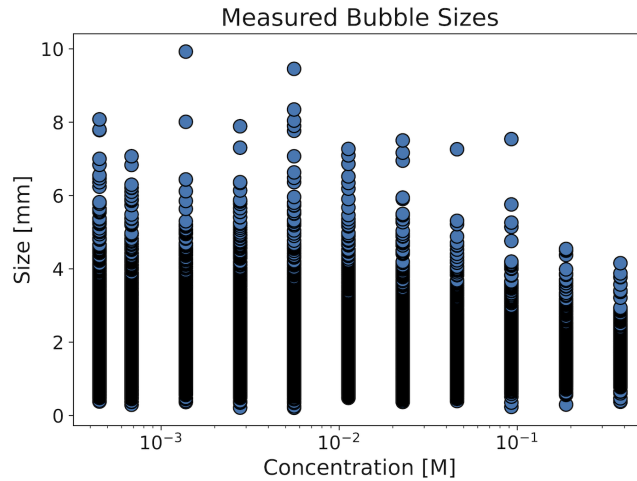


Figure C.2: Histogram of bubble sizes measured by the optical fibre probe.

Means

The mean diameter can be used when the data is (log)normally distributed. At first sight, it can already be seen that the data from above does not have a normal distribution. However, a lognormal distribution could be possible. Normality tests are performed to check whether this statement can be rejected (Table C.1). To reject the null hypothesis, meaning that there is no sufficient evidence to confirm a (log)normal distribution, its p-value needs to be smaller than 0.05.

The results in Table C.1 show that the null hypothesis is rejected in all cases, except one measurement. This means that there is no assurance that the data is lognormally distributed. Rejecting the null hypothesis implies that it is not recommended to use the data's mean for further analysis. The main reason is that outliers, the large bubbles, can significantly influence this value. These outliers cannot be removed as it is unknown whether these points are actual measurements or errors. Also, because the data is not (log)normally distributed, the standard deviation cannot be determined accurately. This causes difficulties when expressing the variation in bubble sizes (Sainani, 2012).

Table C.1: Probabilities from the normality test.

Conc. [M]	p-value [-]
0.0000	7.12e-10
0.0007	2.11e-8
0.0014	2.95e-7
0.003	2.17e-9
0.006	5.01e-15
0.011	9.62e-3
0.023	3.72e-4
0.05	5.45e-1
0.1	7.99e-6
0.2	9.23e-4
0.4	6.45e-7

Within the field of bubble sizes/coalescence, the Sauter mean diameter is also often used. This diameter is most sensitive to the presence of small bubbles within the data distribution and therefore disregards the larger bubbles. This can be useful in suppressing the influence of possible outliers. However, as the experiments aim to study the change in bubble sizes by salts, all bubble sizes should be equally weighted.

Percentiles

The median is generally used when there is no (log)normal distribution. The main advantage of this value is that it is much more robust against outliers (Sainani, 2012). Also, the interquartile range can be used to express the variety in bubble sizes (Figure C.3).

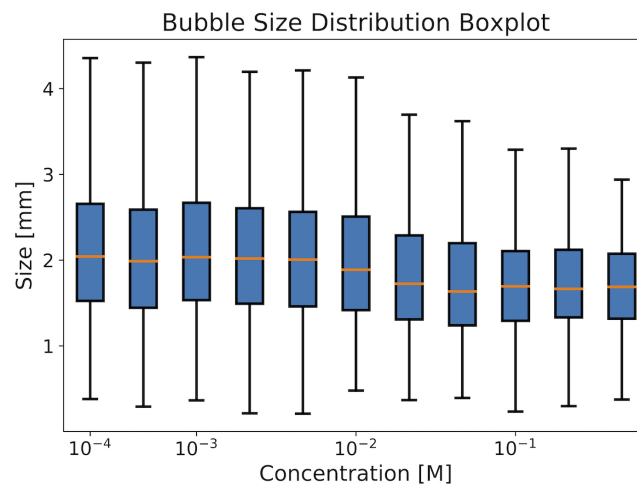


Figure C.3: Boxplot of bubble sizes measured by the optical fibre probe.

To conclude, the mean diameter does not seem an accurate way to represent the largely distributed data. Instead, it is opted to use the median diameter. This results in clear and consistent values for further usage.

D Experimental Workflow

An experimental workflow ensures that all devices and parts are connected properly. Providing this step-by-step approach also makes the setup and results as reproducible as possible. The workflow consists of two parts; building the column and setting up the computer/software.

Column

The column is built by performing the following actions:

1. Connect the gas line with a one-way valve to the bottom port below the column's sparger plate. The one-way valve is connected to only let gas enter the column. Tubing is attached to other equipment by using Swagelok connections.
2. Connect another tube, together with a valve, to the lowest port where water can still access. This tube is used to drain the column when needed.
3. Make sure to close up/plug unused ports. However, do reserve the two highest ports for the fibre probe and pressure sensor. These ports need to be at the same height.
4. Place rubber seal on top of the first column and thereon place the second column. Make sure the holes are aligned. Connect the two columns with screws and thigh them crosswise for optimal fit.
5. Connect the pressure sensor. Do this by first unscrewing the cable connection so that the probe is easy to move/rotate. Remove the red protective cover and insert the probe into one of the reserved ports. Additional tightening can be done by using a wrench. Do however make sure that the connection is not made too tightly as this can damage the ports. Attach the cable to the sensor again.
6. The other port is used to connect the fibre probe to the column. Before doing this, it needs to be checked to see if the probe is clean enough. To do this, remove the protective cover slightly such that the probe is visible but still unable to touch other surfaces. Hold the probe under a microscope to inspect its state. If dirt/particles are visible on the probe, clean the probe from its base to tip with the provided cleaner. To make sure that the movement is straight, so that the tip will not break, use the protective cover as guidance.
7. Once the probe is clean, it can be inserted into the column. This is done by first removing the protective cover, from which the probe can be moved through the port. Make sure the probe is in the middle of the column and pointing downwards. Also here, additional tightening can be done with a wrench. It is always good to mark the positioning of the probe, this allows for more comparable measurements in future experiments.

D Experimental Workflow

8. Once everything is connected, the column can be filled with the desired amount of water. When no measurements are being done, always make sure that a gas flow of 10 L/min is used to prevent water from going through the perforated plate into the gas chamber.

To break down the column, do the above steps in reverse order. In other words, start by shutting down the gas flow and emptying the column of water. End with disconnecting the gas lines.

Computer

The column alone is not enough to perform the experiments, the computer and software also need to be set up:

1. The PC needs to be connected to the flow controller. Here, the airflow going through the column can be adjusted. To do this, start FlowDDE to connect with the controller after which FlowView can be opened.
2. Make sure the pressure sensor is connected to the computer with a National Instruments box. The fibre probe must be connected to the supplied controller unit, which is then connected to the PC. Start LabView and open "Voltage - Continuous Input.vi". Make sure the right channel is selected. This program logs the voltage measured by the pressure sensor.
3. Start "M2 Analyzer for Bubbly flows", this should automatically detect the fibre probe (if the controller is turned on).

E Critical Safety Assessment

Air is bubbled through a water-salt system at a series of salt concentrations to determine their transition concentrations. However, these experiments can only be performed when a clear understanding and evaluation of the risks is done.

E.1 Equipment

To safely handle the equipment mentioned in the [Materials & Methods](#), a solution to different risks has been thought of:

- In case of water overflow of the column, shut off the gas flow. As a drip tray is located under the column, this should result in clean spillage.
- The air comes from a highly pressured system. In case something goes wrong with the flow controller or gas line, always try to leave the room. Contact BHV to secure the room. If the risk is not high or there is no other option, the gas line can be shut off with the green and/or red valve located near the controller. Do, however, make sure that ear protection is used.
- The optical fibre probe measures bubbles based on laser refraction. This probe is assigned to belong to class 1 lasers. According to this classification, the optical fibre probe can be used without extra precautions.

E.2 Materials & Solvents

The usage of NaCl, NH₄Cl, Na₂SO₄ and (NH₄)₂SO₄ has also been evaluated. NaCl and Na₂SO₄ show to be safe for usage as these salts have no dangerous properties. However, NH₄Cl and (NH₄)₂SO₄ show to be irritating. Moreover, these salts can cause the release of ammonia gas when solubilized (Figure E.1).











Temperature (°C)		~20		Pressure (bar)		1-3	
				✓			
							
Hazardous materials and solvents ⁽¹⁾			Dangerous properties ⁽²⁾	TWA 8 hour ⁽³⁾	Halogen rich/poor	Acid /base	Phase ⁽⁴⁾
Sodium Sulfate 7757-82-6			-	-	Poor	-	Liquid
Ammonium Sulfate 7783-20-2			Irritant	17 mg/m ³	Poor	Acid	Liquid
Sodium Chloride 7647-14-5			-	-	Rich	-	Liquid
Ammonium Chloride 12125-02-9			Irritant	17 mg/m ³	Rich	Acid	Liquid

Figure E.1: Risk assessment for salts used during experiments.

E Critical Safety Assessment

The amount of ammonia gas that is released during experiments is calculated by using Henry's law. By considering ammonia gas in equilibrium, this is the maximum amount that can be present in the air from the experimental setup used. At the maximum concentration of 0.5 M ammonium sulfate in the bubble column, a maximum of 1.949 mg/m^3 of ammonia gas can be present in the air. This shows that, even when the room is not ventilated, the ammonia concentration in the air will not exceed the following exposure limits:

- TWA 8 hour = 17 mg/m^3
- STEL = 27 mg/m^3

After performing the experiments, the used materials and solvents also need to be disposed of. Luckily, no special waste disposal is needed as these diluted salts will not harm the environment if under a maximum concentration of 0.5 M. Therefore, the column's content can be disposed of in the sink after experiments.

F Fibre Probe Signal Disturbance

Unlike other salts tested, initial NH_4Cl experiments showed that the fibre probe had problems detecting bubbles as the concentration increased. This problem expanded until the point where the probe could not detect any bubbles at all (Figure F.1).

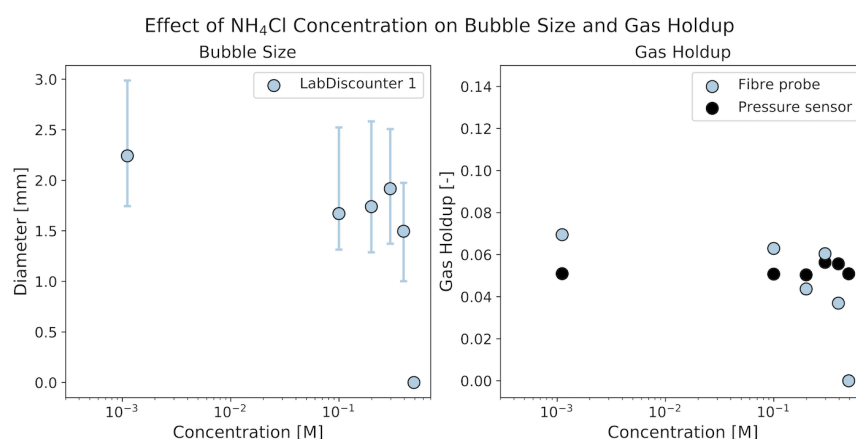


Figure F.1: Effect of NH_4Cl concentration on bubble size (left) and gas holdup (right). Size measurements are represented by their median and interquartile range.

However, this observation appeared unlikely to be caused by NH_4Cl itself. The reason is that previous salts containing NH_4^+ or Cl^- did work on the fibre probe. Therefore, this disturbance would need to be caused by other factors. A potential explanation observed is that the above NH_4Cl resulted in an opaque liquid when solubilized, whereas other salts kept the water clear. To test whether this opaqueness has something to do with the disturbance, three additional NH_4Cl batches have been tested. One of these batches also gives opaqueness, while the others stay clear when NH_4Cl is solubilized (Figure F.2).



Figure F.2: 0.5 M solutions of the different NH_4Cl batches tested. From left to right: LabDiscounter (original), LabDiscounter (other batch), Thermo Scientific and Carl Roth.

As all salts used are not completely pure, they are accompanied by small impurities ($\leq 1\%$). Depending on the salt batch, different impurities can be present. This can cause some batches to (not) result in an opaque liquid when solubilized. Unfortunately, the supplier does not have a detailed description of the impurities published. Therefore, the exact impurity causing opaqueness cannot be identified. When measuring the three different NH_4Cl batches, a clear difference is shown when comparing the results from opaque-inducing and non-opaque-inducing salts (Figure F.3).

One of the main observations from Figure F.3 is that the opaqueness-inducing NH_4Cl batch, from LabDiscounter, shows no consistency between its measured bubble sizes. This inconsistency can be explained as the number of valid bubbles dropped as salt concentration increased. This decreasing number in valid bubbles is due to the NH_4Cl added. The reason is that the baseline measurement is similar to previous baselines. Unfortunately, as size measurements are inconsistent, it is impossible to perform a logistic regression on this data set. Therefore, a transition concentration regime cannot be determined. In addition to these size measurements, the gas holdup is not evolving as expected. In contrast to the relatively consistent pressure sensor measurements, the fibre probe's holdup drops as concentration increases. This is also because the probe is unable to distinguish between the gas and liquid phases when this batch of salt is present.

In contrast to LabDiscounter, the batches from Thermo Scientific and Carl Roth do show consistent measurements in both bubble size and gas holdup. However, it needs to be noted that these measurements are performed with another fibre probe. The reason is that the previous probe did show the potential to measure bubbles at higher salt concentrations, but the measurements varied from time to time. Moreover, the baseline measurement from this probe was off too. This could be due to the fouling of the probe, which was not resolved when cleaning. Even though Thermo Scientific and Carl Roth show a clear bubble transition graph, their results differ quite a lot when comparing the two measurements. Carl Roth's NH_4Cl shows a similar baseline compared to others, whereas Thermo Scientific exhibits a larger bubble size at the baseline and a lower one at the final salt concentration. This difference is hard to explain, especially since the two measurements were performed in two consecutive days. Maybe, as the probe has not been used before, putting it into use for the first time resulted in dissimilar bubble sizes for Thermo Scientific's batch. However, despite their different results, their transition concentrations are relatively the same (see the [Results & Discussion](#)).

Effect of NH_4Cl Concentration on Bubble Size and Gas Holdup

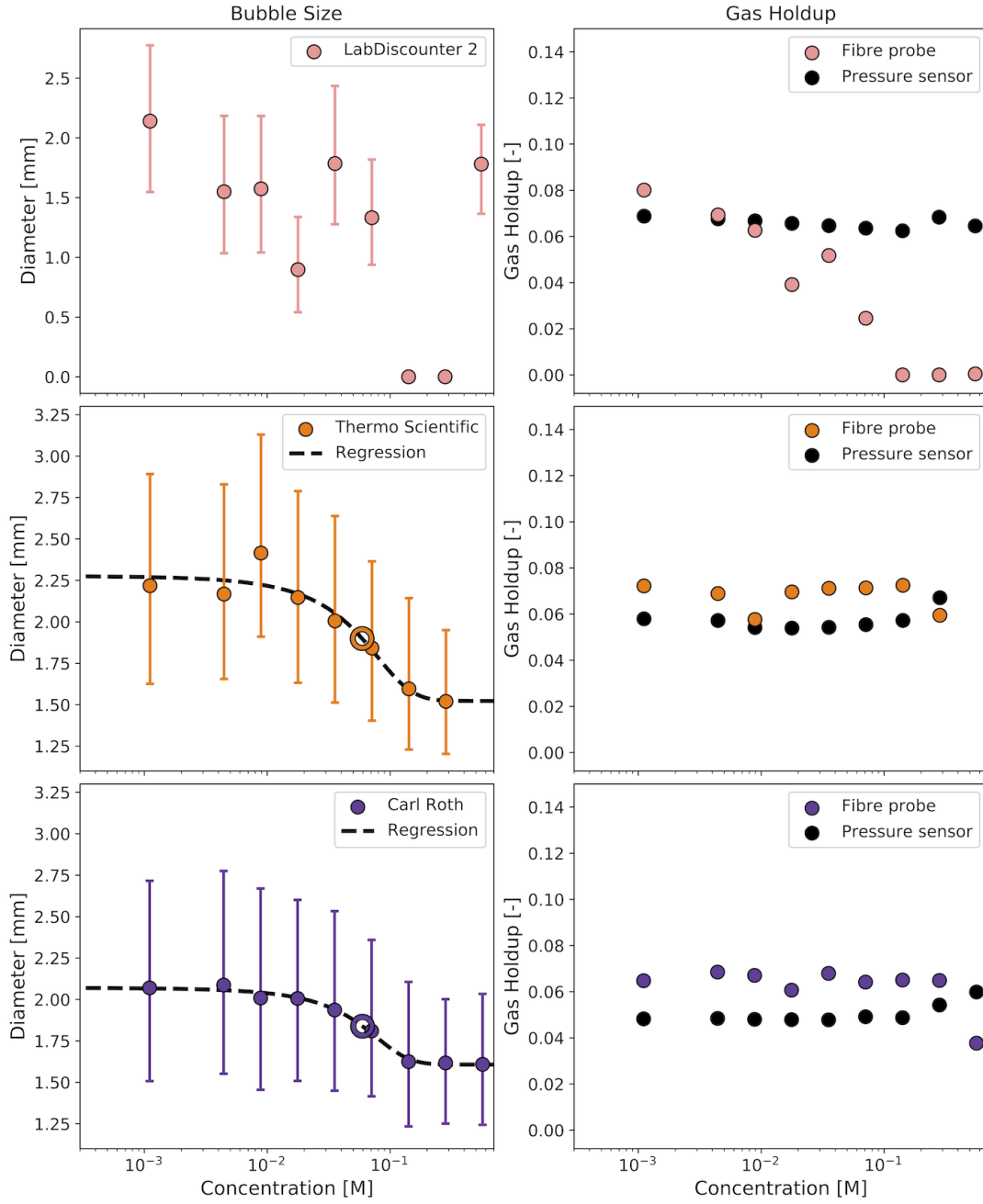


Figure F.3: Effect of salt concentration on bubble size (left) and gas holdup (right). Size measurements are represented by their median and interquartile range. The distinct marker represents a different fibre probe used.

G Transition Concentration

An extensive literature search has been performed to obtain as many transition concentrations as possible (Table 4.3). As can be seen, literature data for $(\text{NH}_4)_2\text{SO}_4$ and NH_4Cl is scarce. Besides, if multiple measurements for the same salt can be found, it shows that these values also largely deviate from each other. These serve as supportive arguments as to why these salts have been tested in this work.

Table G.1: Overview of 50% transition concentrations obtained from literature, together with the measuring technique used to obtain this number.

ⁱConcentration at 95% inhibition. ⁱⁱConcentration at 75% inhibition.

Measuring technique	Source	Salts			
		NaCl	Na ₂ SO ₄	(NH ₄) ₂ SO ₄	NH ₄ Cl
Adjacent capillaries, visual observation	Lessard	0.175	0.061		
	DROGARIS		0.06		
	Zahradnik et al.	0.145	0.051		
	Aguilera et al.	0.1			
	Christenson et al.	0.208			
Bubble column, scattering/light intensity	Nguyen et al.	0.1			
	Craig et al.			0.031	
	Henry et al.	0.078			0.1
Bubble column, size distribution	Quinn et al. ⁱ	0.31	0.13		
	Quinn et al. ⁱⁱ	0.15	0.06		
	Zieminski et al.	0.17			
	Firouzi	0.778			
Thin liquid film, micro-interferometry	Firouzi	0.1			
	Karakashev et al.	0.1			

H Surface Tension Validation

This Appendix shows the actual surface tensions calculated by the model and how much it deviates from the literature. A valid surface tension ($\leq 10\%$) is coloured in green. These values are visualised in the [Results & Discussion](#).

H.1 Pure Electrolytes

Table H.1: Comparing the model surface tensions for NaCl. The transition regime is represented by the values printed in bold.

Conc [M]	Model	Jones and Ray (1941)		Henry et al. (2007)	
	$d\gamma$ [mN/m]	$d\gamma$ [mN/m]	Δ [%]	$d\gamma$ [mN/m]	Δ [%]
0.0001	$4.2 \cdot 10^{-4}$	$-3.6 \cdot 10^{-3}$	111.71	$1.8 \cdot 10^{-4}$	138.75
0.0002	$7.8 \cdot 10^{-4}$	$-7.2 \cdot 10^{-3}$	110.90	$3.5 \cdot 10^{-4}$	122.19
0.0005	$1.8 \cdot 10^{-3}$	$-6.5 \cdot 10^{-3}$	127.40	$8.8 \cdot 10^{-4}$	101.14
0.001	$3.3 \cdot 10^{-3}$	$-7.2 \cdot 10^{-3}$	145.54	$1.8 \cdot 10^{-3}$	85.74
0.002	$6.0 \cdot 10^{-3}$	$-2.2 \cdot 10^{-3}$	379.51	$3.5 \cdot 10^{-3}$	70.99
0.005	$1.3 \cdot 10^{-2}$	$1.0 \cdot 10^{-2}$	33.74	$8.8 \cdot 10^{-2}$	52.73
0.01	$2.5 \cdot 10^{-2}$	$2.4 \cdot 10^{-2}$	1.00	$1.8 \cdot 10^{-2}$	40.06
0.02	$4.5 \cdot 10^{-2}$	$4.9 \cdot 10^{-2}$	7.19	$3.5 \cdot 10^{-2}$	28.69
0.05	$1.0 \cdot 10^{-1}$	$1.1 \cdot 10^{-1}$	7.12	$8.8 \cdot 10^{-1}$	15.91
0.1	$1.9 \cdot 10^{-1}$	$2.0 \cdot 10^{-1}$	5.42	$1.76 \cdot 10^{-1}$	8.01
0.2	$3.6 \cdot 10^{-1}$	$3.9 \cdot 10^{-1}$	7.14	$3.5 \cdot 10^{-1}$	1.87
0.5	$8.5 \cdot 10^{-1}$	$9.0 \cdot 10^{-1}$	5.96	$8.8 \cdot 10^{-1}$	3.81
1.0	$1.6 \cdot 10^0$	$1.7 \cdot 10^0$	5.28	$1.7 \cdot 10^0$	6.48
2.0	$3.2 \cdot 10^0$	$3.5 \cdot 10^0$	6.39	$3.5 \cdot 10^0$	7.99

Table H.2: Comparing the model surface tensions for K_2SO_4 . The transition regime is represented by the values printed in bold.

Conc [M]	Model	Jones and Ray (1937)		Henry et al. (2007)	
	$d\gamma$ [mN/m]	$d\gamma$ [mN/m]	Δ [%]	$d\gamma$ [mN/m]	Δ [%]
0.0002	$1.6 \cdot 10^{-3}$	$-7.2 \cdot 10^{-3}$	121.68	$6.0 \cdot 10^{-4}$	160.20
0.0004	$2.8 \cdot 10^{-3}$	$-1.3 \cdot 10^{-2}$	121.83	$1.2 \cdot 10^{-3}$	135.87
0.001	$6.2 \cdot 10^{-3}$	$-1.8 \cdot 10^{-2}$	135.75	$3.0 \cdot 10^{-3}$	105.95
0.002	$1.1 \cdot 10^{-2}$	$-2.6 \cdot 10^{-2}$	142.92	$6.0 \cdot 10^{-3}$	85.45
0.004	$2.0 \cdot 10^{-2}$	$-1.0 \cdot 10^{-2}$	298.72	$1.2 \cdot 10^{-2}$	66.97
0.01	$4.4 \cdot 10^{-2}$	$2.7 \cdot 10^{-2}$	60.32	$3.0 \cdot 10^{-2}$	46.25
0.02	$8.0 \cdot 10^{-2}$	$8.3 \cdot 10^{-2}$	4.08	$6.0 \cdot 10^{-2}$	33.56
0.04	$1.5 \cdot 10^{-1}$	$1.6 \cdot 10^{-1}$	6.47	$1.2 \cdot 10^{-1}$	23.49
0.1	$3.4 \cdot 10^{-1}$	$3.8 \cdot 10^{-1}$	9.34	$3.0 \cdot 10^{-1}$	14.05
0.2	$6.5 \cdot 10^{-1}$	$6.6 \cdot 10^{-1}$	0.98	$6.0 \cdot 10^{-1}$	9.39
0.4	$1.3 \cdot 10^0$	$1.2 \cdot 10^0$	4.24	$1.2 \cdot 10^0$	6.31
1.0	$3.1 \cdot 10^0$	$2.8 \cdot 10^0$	10.61	$3.0 \cdot 10^0$	3.73

H.2 Electrolyte Mixtures

Table H.3: Comparing the model surface tensions for NaClO₃ + HClO₄.

Conc [M]	Henry et al. (2007) $d\gamma$ [mN/m]	Model $d\gamma$ [mN/m]	Δ [%]
0.022	$-1.5 \cdot 10^{-2}$	$-3.6 \cdot 10^{-3}$	76.51
0.034	$-2.3 \cdot 10^{-2}$	$-1.1 \cdot 10^{-2}$	53.96
0.048	$-3.3 \cdot 10^{-2}$	$-2.1 \cdot 10^{-2}$	36.84
0.057	$-3.9 \cdot 10^{-2}$	$-2.8 \cdot 10^{-2}$	28.41
0.066	$-4.5 \cdot 10^{-2}$	$-3.5 \cdot 10^{-2}$	21.75
0.079	$-5.4 \cdot 10^{-2}$	$-4.7 \cdot 10^{-2}$	13.23
0.089	$-6.1 \cdot 10^{-2}$	$-5.6 \cdot 10^{-2}$	8.02
0.100	$-7.1 \cdot 10^{-2}$	$-6.9 \cdot 10^{-2}$	1.88
0.110	$-7.8 \cdot 10^{-2}$	$-7.9 \cdot 10^{-2}$	2.07
0.120	$-8.3 \cdot 10^{-2}$	$-8.7 \cdot 10^{-2}$	4.73
0.130	$-9.2 \cdot 10^{-2}$	$-1.0 \cdot 10^{-1}$	8.57
0.140	$-9.8 \cdot 10^{-2}$	$-1.1 \cdot 10^{-1}$	11.09
0.150	$-1.1 \cdot 10^{-1}$	$-1.2 \cdot 10^{-1}$	13.96
0.160	$-1.1 \cdot 10^{-1}$	$-1.3 \cdot 10^{-1}$	15.72
0.170	$-1.2 \cdot 10^{-1}$	$-1.4 \cdot 10^{-1}$	18.23
0.190	$-1.3 \cdot 10^{-1}$	$-1.5 \cdot 10^{-1}$	20.37
0.200	$-1.4 \cdot 10^{-1}$	$-1.7 \cdot 10^{-1}$	23.24
0.220	$-1.5 \cdot 10^{-1}$	$-1.9 \cdot 10^{-1}$	25.29
0.240	$-1.6 \cdot 10^{-1}$	$-2.1 \cdot 10^{-1}$	27.45
0.260	$-1.8 \cdot 10^{-1}$	$-2.4 \cdot 10^{-1}$	30.36
0.290	$-2.0 \cdot 10^{-1}$	$-2.6 \cdot 10^{-1}$	32.03
0.310	$-2.2 \cdot 10^{-1}$	$-2.9 \cdot 10^{-1}$	33.77
0.340	$-2.3 \cdot 10^{-1}$	$-3.1 \cdot 10^{-1}$	35.04

Table H.4: Comparing the model surface tensions for NaAc + KClO₃.

Conc [M]	Henry et al. (2007)	Model	
	$d\gamma$ [mN/m]	$d\gamma$ [mN/m]	Δ [%]
0.011	$7.3 \cdot 10^{-3}$	$9.5 \cdot 10^{-3}$	30.13
0.017	$1.1 \cdot 10^{-2}$	$1.3 \cdot 10^{-2}$	17.70
0.023	$1.5 \cdot 10^{-2}$	$1.7 \cdot 10^{-2}$	11.08
0.030	$1.9 \cdot 10^{-2}$	$2.1 \cdot 10^{-2}$	6.84
0.036	$2.4 \cdot 10^{-2}$	$2.5 \cdot 10^{-2}$	4.24
0.043	$2.8 \cdot 10^{-2}$	$2.9 \cdot 10^{-2}$	2.66
0.050	$3.3 \cdot 10^{-2}$	$3.4 \cdot 10^{-2}$	1.72
0.055	$3.7 \cdot 10^{-2}$	$3.7 \cdot 10^{-2}$	1.35
0.063	$4.1 \cdot 10^{-2}$	$4.2 \cdot 10^{-2}$	1.33
0.071	$4.7 \cdot 10^{-2}$	$4.7 \cdot 10^{-2}$	1.49
0.079	$5.2 \cdot 10^{-2}$	$5.3 \cdot 10^{-2}$	1.94
0.087	$5.7 \cdot 10^{-2}$	$5.9 \cdot 10^{-2}$	2.53
0.097	$6.4 \cdot 10^{-2}$	$6.6 \cdot 10^{-2}$	3.52
0.110	$7.1 \cdot 10^{-2}$	$7.4 \cdot 10^{-2}$	4.54
0.120	$7.9 \cdot 10^{-2}$	$8.4 \cdot 10^{-2}$	6.05
0.130	$8.7 \cdot 10^{-2}$	$9.4 \cdot 10^{-2}$	7.39
0.150	$9.7 \cdot 10^{-2}$	$1.1 \cdot 10^{-1}$	9.15
0.160	$1.0 \cdot 10^{-1}$	$1.2 \cdot 10^{-1}$	10.59

H.3 Concentrated Electrolytes

Table H.5: Comparing the model surface tensions for KAc.

Conc [M]	Henry et al. (2007)	Original hydrated radii		10x smaller radii	
	$d\gamma$ [mN/m]	$d\gamma$ [mN/m]	Δ [%]	$d\gamma$ [mN/m]	Δ [%]
0.013	$1.0 \cdot 10^{-2}$	$7.6 \cdot 10^{-3}$	24.30	$7.6 \cdot 10^{-3}$	24.30
0.8	$6.0 \cdot 10^{-1}$	$6.5 \cdot 10^{-1}$	7.02	$6.4 \cdot 10^{-1}$	5.42
0.9	$6.7 \cdot 10^{-1}$	$7.0 \cdot 10^{-1}$	4.52	$6.9 \cdot 10^{-1}$	2.53
1.0	$7.5 \cdot 10^{-1}$	$7.7 \cdot 10^{-1}$	2.20	$7.5 \cdot 10^{-1}$	0.18
1.5	$1.1 \cdot 10^0$	$1.1 \cdot 10^0$	5.97	$1.0 \cdot 10^0$	10.05
2.0	$1.5 \cdot 10^0$	$1.3 \cdot 10^0$	10.94	$1.3 \cdot 10^0$	16.39
2.3	$1.7 \cdot 10^0$	$1.5 \cdot 10^0$	13.07	$1.5 \cdot 10^0$	19.23
2.5	$1.9 \cdot 10^0$	$1.6 \cdot 10^0$	14.34	$1.6 \cdot 10^0$	20.95
2.7	$2.0 \cdot 10^0$	$1.7 \cdot 10^0$	15.39	$1.6 \cdot 10^0$	22.41
2.8	$2.1 \cdot 10^0$	$1.8 \cdot 10^0$	15.94	$1.6 \cdot 10^0$	23.19
2.9	$2.2 \cdot 10^0$	$1.8 \cdot 10^0$	16.40	$1.7 \cdot 10^0$	23.84
3.0	$2.2 \cdot 10^0$	$1.9 \cdot 10^0$	16.87	$1.7 \cdot 10^0$	24.50
3.2	$2.4 \cdot 10^0$	$2.0 \cdot 10^0$	17.74	$1.8 \cdot 10^0$	25.76
3.4	$2.5 \cdot 10^0$	$2.0 \cdot 10^0$	18.49	$1.9 \cdot 10^0$	26.87
3.6	$2.7 \cdot 10^0$	$2.2 \cdot 10^0$	19.24	$1.9 \cdot 10^0$	27.99
3.8	$2.8 \cdot 10^0$	$2.3 \cdot 10^0$	19.85	$2.0 \cdot 10^0$	28.92
4.0	$3.0 \cdot 10^0$	$2.4 \cdot 10^0$	20.44	$2.1 \cdot 10^0$	29.83

Colophon

This document was typeset using \LaTeX , using the KOMA-Script class `scrbook`. The main font is Palatino.

